EXOTIC IONS IN LIQUID HELIUM
IHAS, GARY GENE
ProQuest Dissertations and Theses; 1971; ProQuest Dissertations & Theses Global

72-14,901

IHAS, Gary Gene, 1945-
EXOTIC IONS IN LIQUID HELIUM.

The University of Michigan, Ph.D., 1971
Physics, general

University Microfilms, A XEROX Company, Ann Arbor, Michigan

THIS DISSERTATION HAS BEEN MICROFILMED EXACTLY AS RECEIVED.

Reproduced with permission of the copyright owner. Further reproduction prohibited without permission.

EXOTIC IONS IN LIQUID HELIUM

by

Gary Gene Ihas

A dissertation submitted in partial fulfillment
of the requirements for the degree of
Doctor of Philosophy
(Physics)
in The University of Michigan
1971

Doctoral Committee:

Professor T. Michael Sanders, Jr., Chairman
Professor Otto Laporte (deceased)
Professor Robert R. Lewis
Professor Gabriel Weinreich
Professor Chia-Shun Yih

Reproduced with permission of the copyright owner. Further reproduction prohibited without permission.

PLEASE NOTE:

Some pages have indistinct print. Filmed as received.

University Microfilms, A Xerox Education Company

Reproduced with permission of the copyright owner. Further reproduction prohibited without permission.

ACKNOWLEDGEMENTS

I wish to thank Professor T. M. Sanders, Jr. for giving me the opportunity to do these experiments and calculations. His ideas and assistance on the physics in this work were invaluable.

I thank Professor Gabriel Weinreich for his continued interest, guidance, and encouragement during this work.

I thank Stewart Ryan and George Schofield who are not only good friends but helpful collaborators in the laboratory. I especially wish to thank Stewart for building the electronics for the potassium experiment. The latter experiments on the new negative carriers would not have been run without the full time support of John Magerlein. I thank John for this assistance and pleasant company.

Most of all I wish to thank my wife Irene who aided in every way possible including the typing and assembling of this thesis.

Finally, I thank the U. S. Atomic Energy Commission and the National Science Foundation who provided the funds for this work.

Reproduced with permission of the copyright owner. Further reproduction prohibited without permission.

TABLE OF CONTENTS

	Page
LIST OF FIGURES	v
LIST OF TABLES	vii
CHAPTER I. IONS IN LIQUID HELIUM	1
A. Ion Structures	1
B. Mobility and Friction	2
C. Ion-Roton Scattering	4
CHAPTER II. EXPERIMENTAL METHODS	6
A. Cryogenics	6
B. Mobility Cell	6
C. Time-of-Flight Measurements	7
CHAPTER III. INJECTION AND MOBILITY OF POTASSIUM IONS IN LIQUID HELIUM	14
A. Heavy Ions in He II	14
B. Operation of Hot Wires in Liquid Helium	15
C. Mobility Apparatus	18
D. Data Acquisition and Analysis	20
E. Interpretation of Results	22
CHAPTER IV. EXOTIC NEGATIVE CARRIERS IN LIQUID HELIUM	26
A. Review of Previous Work	26
B. Modifications of K^+ Apparatus	26
C. Preliminary Data and Apparatus Modification	30
D. Data and Analysis	34
E. Possible Models	42
1. Free Electron	42
2. Heavy Impurity Ion	42
3. Excited Electron Bubble State	43
4. Two Electron Bubble	43
5. He^3 Dependent State	43
6. States of He^-	44
F. Conclusion	46

Reproduced with permission of the copyright owner. Further reproduction prohibited without permission.

Page

CHAPTER V. ROTON KINEMATICS AND ION-ROTON SCATTERING 47

A. Introduction 47
B. Classical Roton Mechanics 48
C. Momentum Transfer Cross Section 51

1. General Scattering 51
2. Classical Scattering 53
3. Classical Turning Point 53
4. Anomalous Hard Sphere Scattering 54

D. Particle Fluxes for Hard Sphere Scattering 55
E. Ion-Roton Scattering 61
F. Conclusion 72

APPENDIX I 74

APPENDIX II 75

NOTES 77

BIBLIOGRAPHY 78

Reproduced with permission of the copyright owner. Further reproduction prohibited without permission.

LIST OF FIGURES

Figure		Page
1.	Dispersion curve	3
2.	Experimental cell in Dewar	8
3.	Time-of-flight apparatus	10
4.	Electronics	11
5.	Data traces	12
6.	Hot wire mount	16
7.	K^+ experimental cell	19
8.	K^+ and helium ion velocities	21
9.	K^+ data traces — method two	23
10.	$\frac{\Delta\mu}{\mu}$ vs. temperature	24
11.	Gate pulsing circuit	28
12.	Pulse coupler circuit	29
13.	6.5 cm experimental cell	31
14.	Fast ion data traces	35
15.	Intermediate ion data traces	36
16.	Fast ion velocities	38
17.	Fast ion mobility vs. temperature	39
18.	Intermediate ion mobilities vs. temperature	40
19.	Roton trajectories in a force field	50
20.	Four cases of roton scattering	52
21.	Anomalous hard sphere cross section	56
22.	Anomalous scattering off a plane	58
23.	Cross sections for hard sphere scattering	62
24.	Normal cross sections for $C_4 = 90$	65
25.	Cross sections for $C_4 = 100$	67

Reproduced with permission of the copyright owner. Further reproduction prohibited without permission.

Figure Page

26. Cross sections for $C_4 = 200$ 68

27. Cross sections for $C_4 = 1000$ 69

28. Roton distribution function 71

29. Mass spectrometer 76

Reproduced with permission of the copyright owner. Further reproduction prohibited without permission.

LIST OF TABLES

Table		Page
1.	Ion Data: Slopes and Bubble Radii	41
2.	Cross sections for ion-roton scattering	73

Reproduced with permission of the copyright owner. Further reproduction prohibited without permission.

I. IONS IN LIQUID HELIUM

A. Ion Structures

Charged particles were initially introduced into liquid helium as microscopic probes to investigate the characteristics of the liquid. The injected charges interacted strongly with the liquid creating complexes whose structures formed an interesting subject in itself (Donnelly 1967, chapter 6). K. R. Atkins (1959) predicted that a charge in liquid helium, by polarization and electrostriction of the surrounding helium would be expected to form a solid sphere of some 6 Å radius. This "snowball," and the high density liquid surrounding it, should determine the transport properties of the charge in the liquid — specifically the mobility and effective mass.

For more than a decade only two charge carriers have been examined. These are the positive and negative carriers produced along the ionized track of an α or β particle. It has been adequately demonstrated, both experimentally and theoretically, that the negative carrier is an electron in a bubble. Due to its large zero-point energy and its repulsive interaction with helium atoms, an electron carves a cavity in the liquid. This 16 Å radius cavity prevents formation of the smaller snowball. The positive carrier, although less well investigated, does possess properties which agree with the snowball model. The core ion in this complex is presumed to be a singly charged helium atom or molecule. These pictures have developed from studies of the

Reproduced with permission of the copyright owner. Further reproduction prohibited without permission.

ion mobilities as a function of temperature and pressure (Schwarz and Stark 1968, 1969 and Brody 1970), effective mass (Dahm and Sanders 1966, 1970), photo-ejection (Zipfel 1969, Zipfel and Sanders 1969, and Miyakawa and Dexter 1970), and ion trapping on vortex lines (Douglass 1964, Cade 1965, and Parks and Donnelly 1966). This thesis describes the investigation of several new ion complexes in He II through mobility measurements.

B. Mobility and Friction

One of the simplest measurable properties of a charge carrier is its drift velocity v through a medium under the influence of an applied electric field $\mathcal{E}$. For sufficiently weak electric fields, the carrier will reach a terminal velocity proportional to the electric field strength. We can then write $e\mathcal{E} = \gamma v$, where we will call γ the friction coefficient. Alternatively, we may write $v = \mu \mathcal{E}$, where μ is called the mobility. The quantities γ and μ are connected by the relation $\gamma = \frac{e}{\mu}$.

The mobility of an ion in He II (the superfluid phase of liquid helium) is determined by scattering with elementary excitations. These elementary excitations follow the dispersion curve $\varepsilon(k)$ shown in Fig. 1 (after Yarnell, Arnold, Bendt, and Kerr 1959). This curve has a linear phonon region and a minimum at $k = 1.92\ \text{Å}^{-1}$, at which the energy is 8.68K. The excitations which occupy this dip are called rotons, and the energy at the minimum is called Δ, the roton energy gap. In the temperature range

Reproduced with permission of the copyright owner. Further reproduction prohibited without permission.

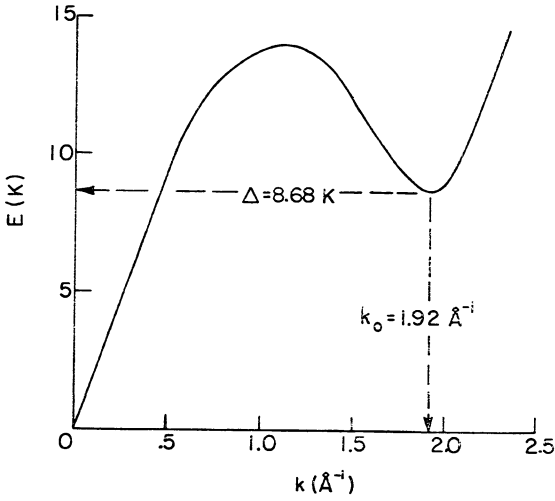

Fig. 1. Dispersion curve for elementary excitations in He II. The momentum and energy of the roton minimum are shown. The data are for T≈1.15K.

Reproduced with permission of the copyright owner. Further reproduction prohibited without permission.

from about 1K to 2K rotons determine the friction experienced by a particle moving through the liquid.

The best treatment of the transport problem has been given by Baym, Barrera, and Pethick (1969). They assume the carrier to be so massive that its velocity change in a single collision can be neglected. The ion masses are known to be large but no test has been made of the dependence of the mobility on mass, and the applicability of the infinite mass theory. In the present experiments, we measure the mobility of a new positive ion, K^+, in an attempt to study this point. The theoretical expression for the mobility involves only one unknown quantity, the momentum transfer cross section for ion-excitation collisions.

C. Ion-Roton Scattering

The cross sections for ion-roton scattering have not been investigated theoretically in the literature. In the analysis of experimental data, it has usually been assumed that the cross section is independent of roton momentum (Careri, Scaramuzzi, and Thomson 1959, Reif and Meyer 1960, Kuper 1961, and Arkhipov 1966). Some authors have taken it to be basically a geometrical cross section, $\pi(R+d)^2$, where R is an ion radius, and d an effective roton size (Schwarz and Stark 1969). Although such an assumption yields the correct temperature dependence for the mobilities, the magnitudes of the cross sections are difficult to understand. In fact, the cross section for

Reproduced with permission of the copyright owner. Further reproduction prohibited without permission.

the negative carrier is only one fourth of the geometrical cross section (πR^2) calculated from other, independent, determinations of the bubble radius. For the positive carrier, on the other hand, the indicated cross section is approximately twice geometrical (πR^2), if the radius is evaluated from independent sources. This discrepancy in cross sections is shown quite vividly when one examines the pressure dependence of the mobilities. The two mobilities – and presumably the cross sections – become equal when an external pressure of about 100 psi is applied (Brody 1970). Yet, independent data indicate that the carrier radii are very different at this pressure. These considerations indicate that an examination of the subject of ion-roton scattering is needed. We present our efforts in this connection in Chapter V.

Reproduced with permission of the copyright owner. Further reproduction prohibited without permission.

II. EXPERIMENTAL METHODS

A. Cryogenics

The experiments are performed in a conventional strip-silvered glass Dewar pair. Temperatures down to 1.2K are produced by pumping with an 80 cfm Stokes Model 149H mechanical pump. A Stokes Model 900-150-1 (4 inch) booster diffusion pump lowers the temperature to 0.95K.

The vapor pressure in the experimental cell is measured through a half inch lead tube which is a static line. Thermo-molecular corrections are negligible above 1.1K; they have been applied at lower temperatures. Temperatures are derived from the vapor pressure using the 1958 He^4 scale.

A carbon resistor is calibrated against the vapor pressure and used as a convenient secondary thermometer. We use a 1/10W, 100Ω Allen-Bradley resistor, conducting a small enough current to avoid self-heating, which goes from 1 kΩ at 4K to 200 kΩ at 1K. The resistance vs. temperature data are fitted to the equation

$$T^{-1} = a + \frac{b}{\log R} + c \log R$$

which is used to generate a table of resistance values and temperatures. The stability of the resistor's calibration is checked in each run.

B. Mobility Cell

The time-of-flight cell consists of an electrode

Reproduced with permission of the copyright owner. Further reproduction prohibited without permission.

structure contained in a glass and metal can. This experimental cell, shown in Fig. 2, is suspended from the pumping head at the top of the Dewar by a length of half-inch, thin-walled, copper-nickel tubing. Electrical connections to the cell are made through this lead tube via low heat-conductivity wire. Room-temperature hermetic electrical feed-throughs and a gas connection for vapor pressure measurements are mounted at the top of the lead tube.

The liquid level in the experimental cell is controlled separately from the level in the Dewar by filling the cell through a modified Hoke valve[1]. The stem of the cryogenic valve is brought to room temperature using a stainless steel tube three feet long. The experimental can has a glass portion sealed between two copper sections, permitting visual observation of the electrode structure. The lead tube and valve stem pass through the pumping head using "O" ring seals, so that the entire apparatus can be moved vertically in the Dewar. In our later experiments, a brass bellows was incorporated into the experimental can. This allowed us to adjust the liquid level in the cell without adding or removing any material. The bellows rested on the bottom of the Dewar, and was cushioned by styrofoam.

C. Time-of-Flight Measurements

Drift velocities can be measured by several techniques, the most straightforward being to measure the time a charge

Reproduced with permission of the copyright owner. Further reproduction prohibited without permission.

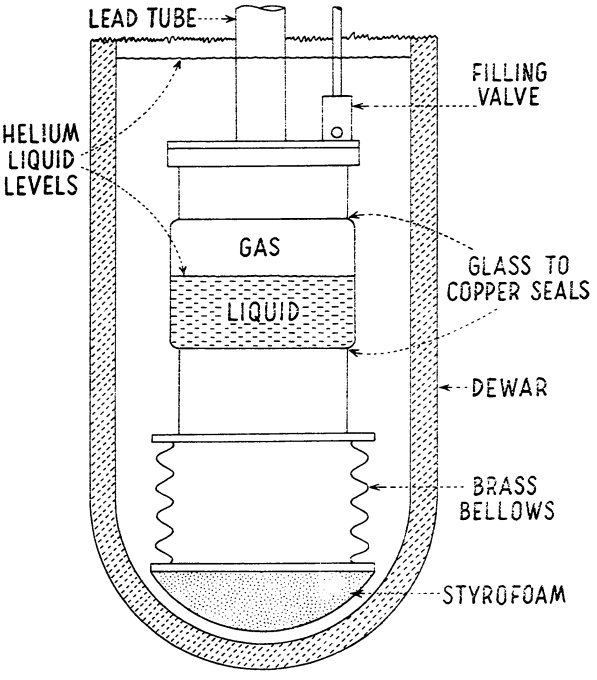

Fig. 2. The experimental cell in the helium Dewar, showing the filling valve and the bellows used to adjust the liquid level in the cell. For clarity, the electrode structure is not shown inside the glass and metal can.

Reproduced with permission of the copyright owner. Further reproduction prohibited without permission.

takes to traverse a known distance under the influence of a uniform electric field.

The single-gate time-of-flight apparatus used in these experiments (Fig. 3) is designed to measure drift velocities. Voltages are applied to the electrodes so that charge carriers are drawn away from the ion source S, periodically chopped into small packets in the gate (grids G1 and G2), moved across the drift region from G2 to G3 by a potential difference V, and detected at the collector C. Electrodes H1, H2, and H3 are drift field homogenizers, and G3 is a Frisch grid, which makes the detected ion pulse more sharply defined. The time between the gate pulse and the following ion pulse is the ion's transit time t across the drift region of length ℓ. Since $v = \frac{\ell}{t}$ and $\mathcal{E} = \frac{V}{\ell}$ we obtain $\mu = \frac{\ell^2}{Vt}$ or $\gamma = \frac{eVt}{\ell^2}$.

A block diagram of the cell and signal electronics is shown in Fig. 4. The voltage V is measured using a digital voltmeter. Ion signals are detected using a fast electrometer, and the signal-to-noise ratio is improved by signal averaging. Final data traces are recorded for analysis using an X-Y plotter. The signal averager sweep is calibrated using a square wave of known frequency, from a frequency counter.

A typical data trace, together with the gate reference pulse and a time calibration trace are shown in Fig. 5. The spikes at a and b correspond to the edges of the gate

Reproduced with permission of the copyright owner. Further reproduction prohibited without permission.

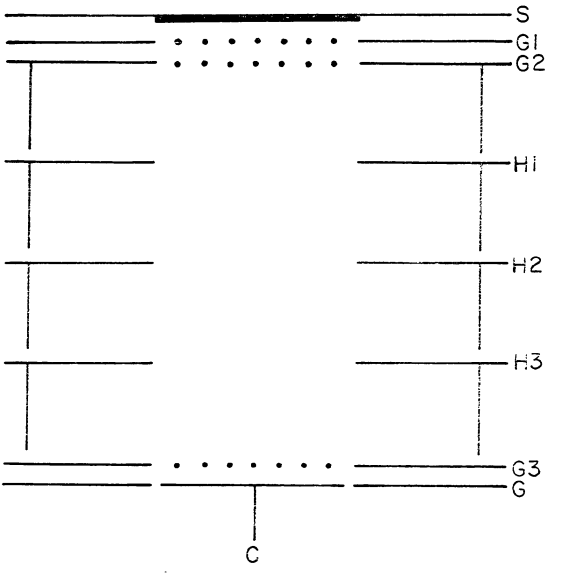

Fig. 3. Diagram of the time-of-flight apparatus. S is the source plane (a radioactive source is shown). Grids G1 and G2 define the gate region, and G2 and G3 define the drift region. Field homogenizers H1, H2, and H3 have rings attached to exclude stray fields. The collector C has a grounded guard ring G, the region from G3 to G being the Frisch region. Ions are created at S and ultimately detected at C.

Reproduced with permission of the copyright owner. Further reproduction prohibited without permission.

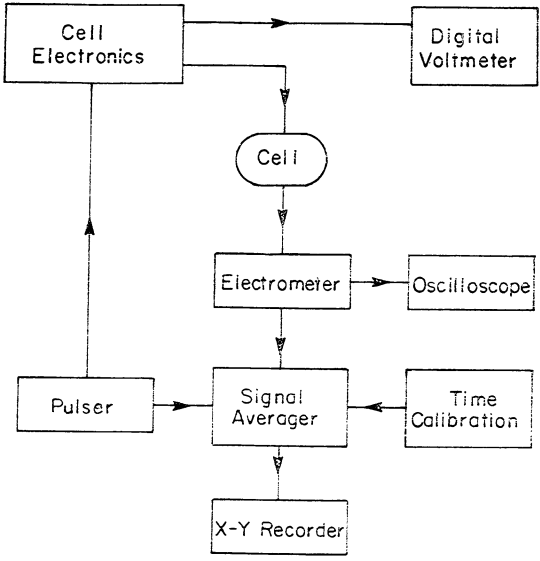

Fig. 4. Block diagram of the electronics for time-of-flight ion experiments.

Reproduced with permission of the copyright owner. Further reproduction prohibited without permission.

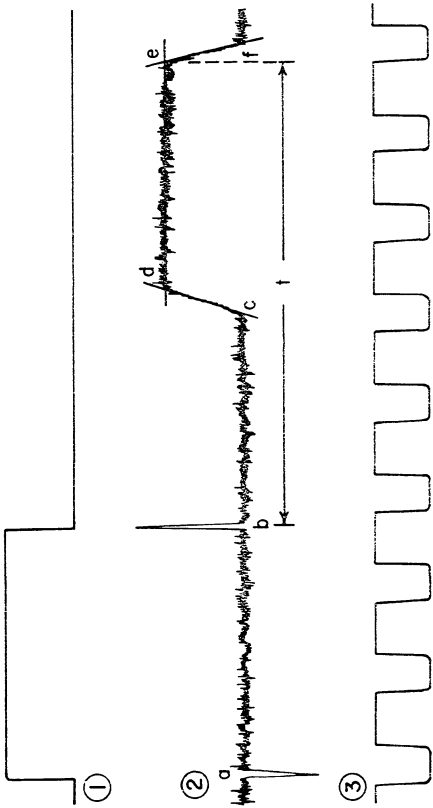

Fig. 5. Draftsman's copies of typical data traces: (1) is the gate pulse; (2) is an ion current pulse for positive carriers; and (3) is a square wave of known frequency which is fed into the signal averager to calibrate the horizontal (time) axis.

Reproduced with permission of the copyright owner. Further reproduction prohibited without permission.

pulse, and are picked up in the cell. The trapezoidal ion pulse has three distinct parts: the slope (c-d) is the time required for the leading edge of the pulse to traverse the collector region (G3 to C); the plateau (d-e) represents the time charge fills the collector region; the slope (e-f) represents the trailing edge of the packet of charge traversing this region. The time (t) from b to e is the transit time across the drift region (G2 to G3). It is used in conjunction with the applied drift voltage (V) and the measured drift-region length (ℓ) to calculate the mobility.

The experimental procedure is to measure ion transit times as a function of drift voltage and temperature. At a given temperature the ion velocities are plotted vs. drift electric field to insure that the measurements are taken on the linear portion of this curve (see Figs. 8 and 16). The slope of this straight line yields the mobility. Ideally, the weak-field mobility can be derived from a single data point if the ion velocity is kept low enough. This procedure was often used in the following experiments.

Reproduced with permission of the copyright owner. Further reproduction prohibited without permission.

III. INJECTION AND MOBILITY OF POTASSIUM IONS IN LIQUID HELIUM

A. Heavy Ions in He II

One consequence of the Atkins model, in conjunction with the Baym, Barrera, and Pethick mobility theory, is that the mobility of a heavy ion in He II will depend only on the charge of the ion, and not its mass. This prediction has not been checked because only one ion has been studied. Cold (tunneling) cathodes (Onn and Silver 1971), field emission points (Mc Clintock 1969 and Hickson and Mc Clintock 1971), photo-injection (Dahm, Levine, Penley, and Sanders 1961), and hot wires (Spangler and Hereford 1968) have been used to inject electrons into the liquid. Ionization due to radioactive sources immersed in the liquid (Williams and Stacey 1957 and Arkhipov and Shal'nikov 1960) and glow discharges in the vapor (Date, Hori, and Kamata 1971) have been used to produce both positive and negative carriers. None of these experiments has tested the dependence of the mobility on ionic mass, since only positive helium ions and electrons are produced.

We have checked this prediction of the Atkins model by studying the mobility of singly charged potassium ions in He II (Ihas and Sanders 1970). That is, we have produced an ion complex in He II which has the same charge as the positive helium ion, but which has a core mass ten times that of a He^+ ion. We measure mobilities and derive values

Reproduced with permission of the copyright owner. Further reproduction prohibited without permission.

for $\frac{\Delta\mu}{\mu} = \frac{\mu_{He} - \mu_K}{\mu_{He}}$, the relative difference in ionic mobilities. If the Baym, Barrera, and Pethick theory is applicable and both ions produce snowballs of the same size then the mobilities will be equal.

B. Operation of Hot Wires in Liquid Helium

Potassium ions are injected into the liquid using a 7 μm diameter tungsten filament (G. E. type 218), submerged in the liquid, and heated to incandescence by an electric current. We first used hot wires to repeat the work of Spangler and Hereford, who used heated tungsten filaments to inject electrons into He II. We mounted the filament between two tinned copper studs using silver conducting paint. The studs were molded into an epoxy[2] block for mounting in the cell (see Fig. 6).

The wire has a resistance of about 2 ohms when immersed in liquid helium. In He I, before the wire becomes incandescent, bubbles stream away from the wire and the wire breaks. The behavior is different when the wire is heated in He II. Until a critical heater current is reached, the wire remains approximately in thermal equilibrium with the helium bath. Above this threshold current the wire heats and its resistance and the voltage across it rise rapidly. The hot resistance of the wire is about 100 ohms. The wire can be continuously heated with a relatively small power dissipation because a layer of vapor surrounds the hot part of the wire (Lemieux and Leonard 1968). To have stable operation when the wire resistance

Reproduced with permission of the copyright owner. Further reproduction prohibited without permission.

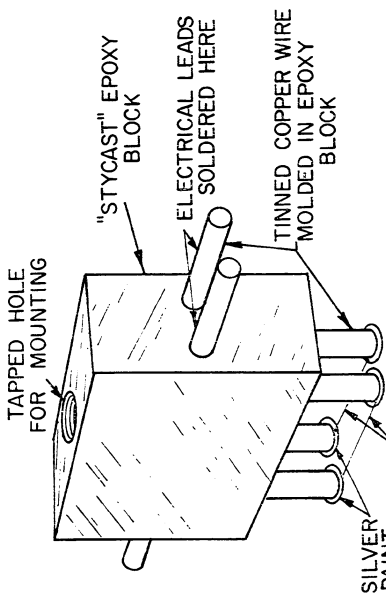

Fig. 6, Detail of the tungsten wire mounts.

Reproduced with permission of the copyright owner. Further reproduction prohibited without permission.

jumps, the heater current is supplied using a voltage regulated, dc power supply and a 15 ohm series resistor. With this resistance value, the power dissipated in the wire will not change when the bubble forms. As the depth of the wire in the liquid is increased, the power needed to create the bubble increases. At a depth of 26 cm, a rumbling noise (Lemieux and Leonard 1968) can be heard outside the Dewar! To investigate this effect we installed a ceramic microphone under the liquid to monitor the sounds produced. By varying the temperature, wire depth in the liquid, and heater power, the noise was found to be an indicator of bubble instability – louder noises indicating greater instability. The bubble was most stable when the liquid level over the hot wire was small. The wire was therefore operated a few millimeters below the liquid-vapor interface, and dissipated only a few milliwatts. Negative currents as large as 10^{-8} amp were measured.

A potassium-doped tungsten wire can be used as an ion source, because when the tungsten is heated, potassium boils off in ionic form, leaving an electron behind[3]. This occurs because the work function of tungsten (4.55 ev) is larger than the first ionization potential of potassium (4.33 ev). General Electric type 218 tungsten filament wire is doped by the manufacturer with approximately 100 ppm of potassium to reduce grain growth. The positive ion current produced by these hot wires was as large as 10^{-12} amp in He II. This current was found to be K^+ by doing

Reproduced with permission of the copyright owner. Further reproduction prohibited without permission.

mass spectrometry on the emissions from the wires. (For further details see Appendix II.)

C Mobility Apparatus

The experimental cell is shown in Fig. 7. The hot wires are mounted at the upper end of the electrode structure. A Po^{210} source is mounted next to them to produce positive helium ion complexes. The bellows had not yet been incorporated into the experimental can. The cell was filled with He II until all exposed leads and the two sources were just covered. The glass portion of the cell permitted visual observation of the filling process and the hot wire operation.

All electrodes and grids[4] are nickel: the grids are spot welded to their holders. The electrodes are held in place with three notched nylon supports which were cut from a single notched block. The collector is a brass disc, soldered to the center pin of a Microdot printed circuit connector[5], whose body is soldered to a guard ring. This whole assembly is then gold plated; the Teflon insulation in the connector does not plate. Microdot low-noise cable[6] is used to bring the collector signal to room temperature.

To measure the mobility of K^+ the heated filament is forward-biased while the radioactive source is back-biased. These biases are reversed when studying helium ions, but the filament is kept hot so that conditions in the cell remain the same. These bias voltages were kept below 20 volts to prevent ionization of the helium gas in the bubble

Reproduced with permission of the copyright owner. Further reproduction prohibited without permission.

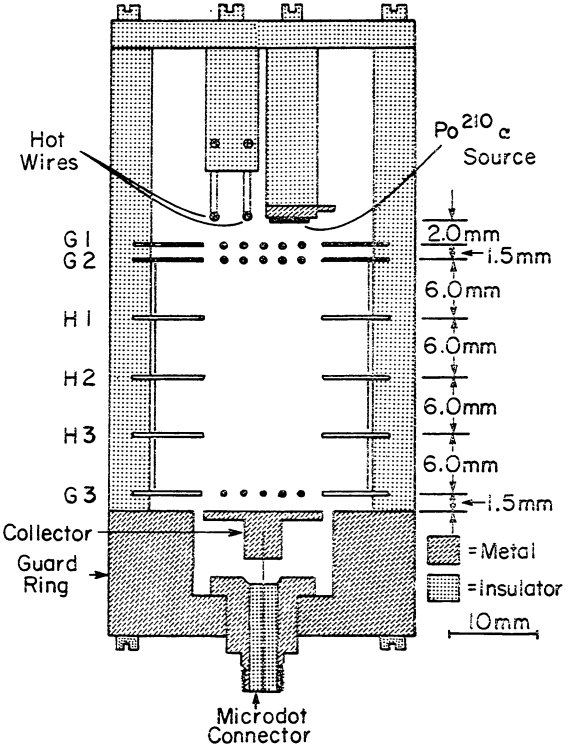

Fig. 7. The K^+ experimental cell showing the two sources positioned at the top, the grid and electrode structure, and the collector assembly. The Microdot connector is not to scale.

Reproduced with permission of the copyright owner. Further reproduction prohibited without permission.

around the hot wire. The region between G1 and G2 is normally reverse-biased. A mercury-wetted relay, driven by a pulsing circuit, periodically applies a short forward-bias which admits a packet of charge into the drift region. The relay allowed the gate pulse to float on the drift and Frisch voltages. As the charge passes the Frisch grid (G3), it is seen by the collector and detected by a fast electrometer.

D. Data Acquisition and Analysis

Two different methods were used to detect and measure what turned out to be quite small mobility differences. In method one we measure one ion mobility and then, as soon as possible, the other. Signal-averaging each ion takes about 4 seconds; recording the resulting trace on an X-Y plotter requires 15 seconds. The two data traces which are later compared can be taken within one minute. The order in which the two ion signals were averaged was changed to check for procedural hysteresis and drifts; none were detected. Velocities for both the K^+ and helium ion complexes are plotted vs. drift electric field for two temperatures in Fig. 8. Note the linearity of the data, and the small but detectable difference in mobility between the two ions.

Method two determines $\Delta\mu/\mu$ by studying the result of subtracting the two ion signals electronically. After a number of pulses from one ion source is added to the memory of the signal averager, an equal number from the other

Reproduced with permission of the copyright owner. Further reproduction prohibited without permission.

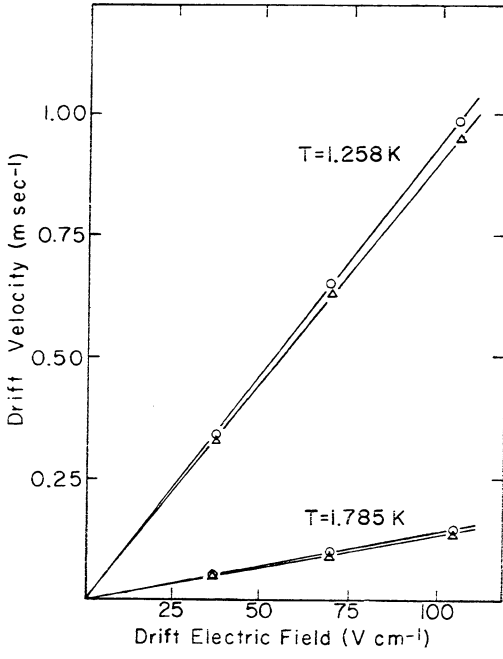

Fig. 8. Ion velocity v plotted against drift electric field $\mathcal{E}$ at two temperatures. Triangles are K^+ and circles are normal helium ions.

Reproduced with permission of the copyright owner. Further reproduction prohibited without permission.

source is subtracted. This eliminates the time delay due to recording the averaged signal from the first ion type. Figure 9 shows an example of data taken in this way. The transients at the beginning and end of the ion pulse are studied to determine $\Delta\mu/\mu$. The precision of this method is limited by the non-ideal shape of the signal pulses. However, this is an inherently better method than method one, and it does show clearly that there is a difference in the mobilities of the potassium and helium ion complexes. The sign of $\Delta\mu/\mu$ was always positive using this second technique.

The temperature dependence of $\Delta\mu/\mu$, derived using both methods, is shown in Fig. 10. No difference in mobility was detected when the same ion source was used in both steps of method two. Both methods yield the same mobilities for the negative carriers from the two sources. This is reassuring, since the negative complex is known to be sensitive to turbulence and supercritical flow (Careri and Scaramuzzi 1961 and Cope and Gribbon 1967), which might be expected around the hot wire. In view of the checks we have made, we are convinced that the small measured mobility difference between the K^+ and helium ion is real.

E. Interpretation of Results

The data show that the mobility of an ion in He II is only weakly dependent on the core ion mass. Changing the mass of the core ion an order of magnitude has affected the mobility of the complex by only a few percent. The heavier

Reproduced with permission of the copyright owner. Further reproduction prohibited without permission.

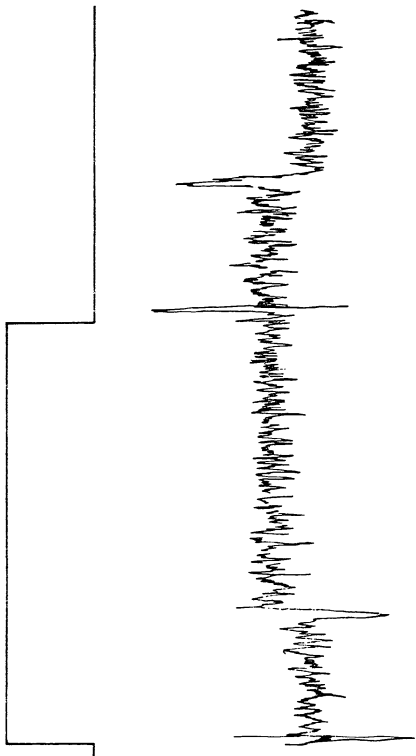

Fig. 9. Draftsman's copies of experimental data traces. The upper trace is the gate pulse and the lower trace shows data taken using method two. The trace is offset between the transients because the K and helium ion signal have different amplitudes. In this case the K signal was added in the memory and the helium ion signal was subtracted. The trace length represents 0.5 sec.

Reproduced with permission of the copyright owner. Further reproduction prohibited without permission.

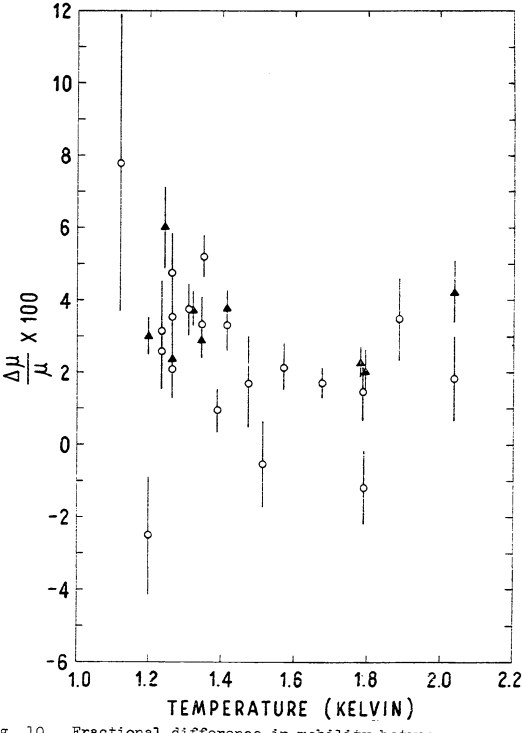

Fig. 10. Fractional difference in mobility between potassium and normal helium ions. The circles are for data taken using method one, and triangles represent data taken using method two.

Reproduced with permission of the copyright owner. Further reproduction prohibited without permission.

core ion increases the effective mass of the ion complex, and decreases its mobility. The helium ion complex is known to have an effective mass of from 30 to 40 helium masses (Dahm and Sanders 1966 and 1970). The K^+ complex should then have an effective mass some 30% larger. The insensitivity of the mobility to the ion mass is in general agreement with the Atkins snowball model and the infinite mass theory. A coincidental compensation of effects of cross section and mass changes would not be detected in these mobility measurements. At present there is no published theory of the mobility of an ion with finite mass[7]. A quantitative comparison of the measured values of $\Delta\mu/\mu$ with theory is not possible.

Reproduced with permission of the copyright owner. Further reproduction prohibited without permission.

IV. EXOTIC NEGATIVE CARRIERS IN LIQUID HELIUM

A. Review of Previous Work

Many workers have studied the two "normal" carriers in liquid helium during the last decade. Recently Doake and Gribbon (1969) reported discovery of a new negative carrier, with a mobility substantially higher than that of either normal carrier. In their experiments Doake and Gribbon produced normal and fast negative carriers using Po^{210} and Am^{241} α sources (presumably immersed in the liquid). They measured velocities by the method of Cunsolo (1961), at fairly high electric fields. By measuring the velocity of the fast ion as a function of electric field, they found that it did not produce vortex rings; the ion velocity was limited at about 50 meters/sec, apparently by the creation of rotons (Rayfield 1968).

We have verified their discovery, extended their measurements to weaker electric fields and to higher temperatures, and performed experiments to probe the nature of the new charge carrier (Ihas and Sanders 1971). We have also discovered the existence of a large family of negative charge carriers, and shown the usefulness of a weak electrical discharge in the vapor above the liquid as a source of ions.

B. Modifications of K^+ Apparatus

After some modification, the apparatus from the potassium ion experiment was used to study the fast negative

Reproduced with permission of the copyright owner. Further reproduction prohibited without permission.

ion. All nickel electrodes and grids were gold plated. A 1/4 Ci tritium β source, mounted on a gold plated disc, was used in place of the hot wires and Po^{210} α sources. A Stokes 4-inch booster diffusion pump, connected between the Dewar pumping head and the mechanical pump, extended the temperature range to 0.95K. Doake and Gribbon had indicated that the fast ions were only detectable below 1.05K.

Due to the high mobility of these ions, the relay pulsing scheme used previously was not suitable. The turn-on and turn-off times were longer than the shortest transit time of the new species across the drift region. The new pulsing circuit, using a photon coupler for isolation, is shown in Fig. 11. Commercial power supplies are used with this circuit, and for all other voltages applied to the cell except the source voltage. Batteries are used for the source voltage, in order to minimize capacitance to ground. The complementary output transistors can deliver pulses up to 250 volts, and draw current only while switching. In operation, switching times are less than 10 μsec. The output of the pulsing circuit is applied between grids G1 and G2 to gate the ions in the cell. The voltage on G1 is read into the signal averager for reference purposes, using the pulse coupler shown in Fig. 12. This circuit allows the connection of ground potential electronics (such as an oscilloscope and signal averager) to the pulsed grid of the cell without slowing the switching times. Due to the large

Reproduced with permission of the copyright owner. Further reproduction prohibited without permission.

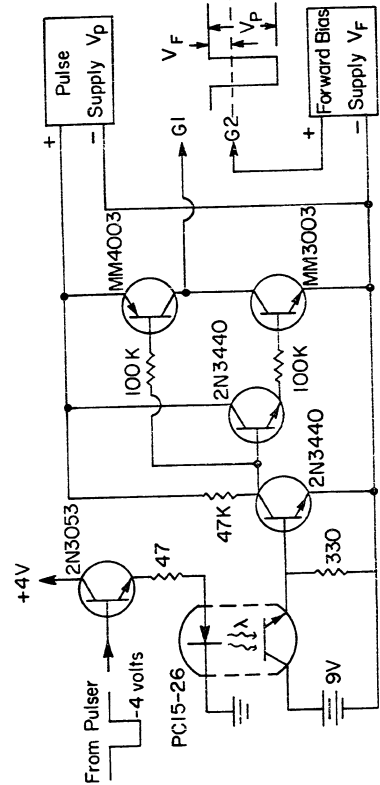

Fig. 11. Circuit to control the cell's ion gate (grids G1 and G2). The photon coupler (PC 15-26) isolates the high voltage pulsing circuit, including the two 0-250 volt power supplies V_P and V_F, from the grounded pulser, enabling the gate to be floated on the drift and Frisch region voltages. (Photon coupler is made by General Electric and the MM transistors are made by Motorola.)

Reproduced with permission of the copyright owner. Further reproduction prohibited without permission.

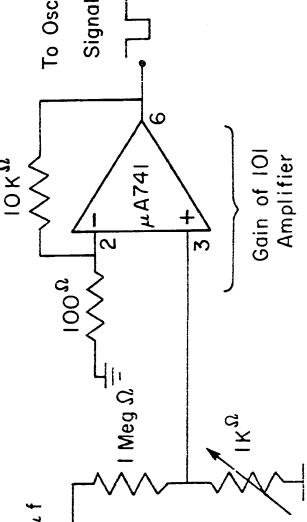

Fig. 12. Schematic of the pulse coupler. The over-all gain is variable from 0 to 1/10. The operational amplifier is by Fairchild.

Reproduced with permission of the copyright owner. Further reproduction prohibited without permission.

RC time constant of the circuit, it gives a true picture of quite long pulses. A Fabri-Tek model 1062 signal averager with 1024 channel memory, capable of sweeping as fast as 4 μsec per channel, made time resolution of the fast ions very easy.

In order to facilitate more accurate mobility measurements, a cell with a longer (6.5 cm) drift region was built. The electrodes and guard rings were contained in a nylon tube with the collector at one end and the source (discussed later) at the other. A cross sectional diagram is shown in Fig. 13. Good ion data were obtained using this long cell, but the signal was always weaker than in the short cell. This may be due to two factors: (1) the drift field is less homogeneous, since fewer field homogenizers per unit length are used; and (2) the center hole in the electrodes, which the ions travel through, is 50% smaller in area than in the short cell. To check that the signal attenuation was due to the design, and not the length of the long cell, a cell the length of the original cell (2.6 cm) was built exactly like the long cell. All long cell parts were used except for the outer nylon tube, which was shorter. This cell then had only one field homogenizer. It produced signals with the same size and shape as the long cell, but with shorter transit times.

C. Preliminary Data and Apparatus Modification

Our initial experiment with the fast ions was to reproduce the conditions of Doake and Gribbon. We did not

Reproduced with permission of the copyright owner. Further reproduction prohibited without permission.

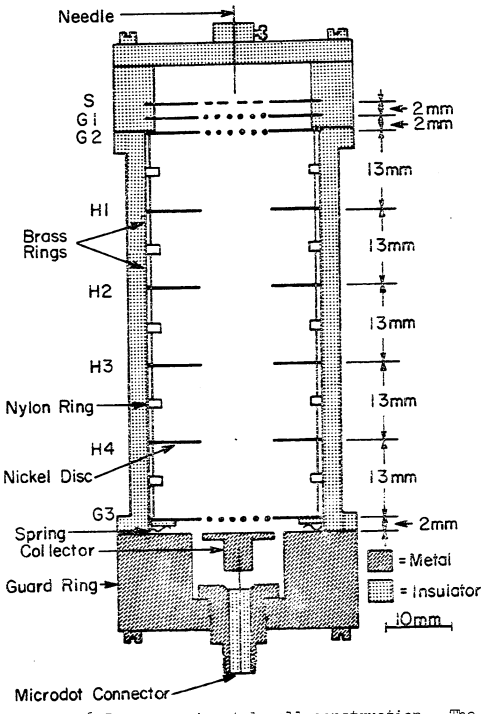

Fig. 13. The 6.5 cm experimental cell construction. The shower head I source is shown in place. The spring compensates for the differential contraction of the brass rings (used to shield out stray fields) and the nylon tube. The same collector assembly is used in all cells.

Reproduced with permission of the copyright owner. Further reproduction prohibited without permission.

know many details of their cell arrangement (e.g. whether their α source was at the top or the bottom), nor were we using an α source. Using the relatively high source and drift-region fields they described, we could roughly reproduce the dc voltage-current characteristics they reported. However, when the cell was pulsed, the intensity of the fast ion signal varied widely from run to run. It sometimes appeared with strength comparable to the normal ion signal, sometimes was very weak, sometimes was undetectable, and did not seem to correlate systematically with the variables we were changing deliberately.

A catalogue of the various experimental runs revealed that the fast ion signal strength was directly related to the liquid level. In fact, the fast carrier was undetectable unless the liquid level was less than 3 mm above the source. When voltages were applied to the cell, visual inspection revealed that the liquid meniscus distorted near the source. The signal appeared only when the liquid surface came into contact with the source, at which point the surface took on an unstable appearance. Best signals were seen when a visible glow discharge appeared in the vapor. At this point we had only observed the fast ion pulses for rather high values of source and drift electric fields, such as those used by Doake and Gribbon. But these were needed only to produce the large surface distortion and glow discharge and were not an inherent property of the carriers.

With our knowledge of the importance of the glow

Reproduced with permission of the copyright owner. Further reproduction prohibited without permission.

discharge and the liquid level, the apparatus was modified in the following ways. The bottom of the experimental can was replaced with a bellows (Fig. 2). This arrangement allowed quick and reversible level changes, leaving the cell closed. Also, the "shower head I" discharge source was constructed, as shown in Fig. 13, and used in both short and long cells. With the needle grounded, and the perforated disc at the source potential (with some megohms of series resistance), the "shower head" produces a glow discharge in the vapor, dissipating only a few milliwatts. Best results are obtained using a sharp, tungsten needle, whose tip is located a few thousandths of an inch above the perforated disc. In later runs, a lucite tube, surrounding the needle and running from the needle mount to the perforated disc, was added to confine the glow discharge. The entire source with lucite tube is called "shower head II."

With the liquid level at the perforated disc, fast ion signals as large as 10^{-11} amp are readily produced, at temperatures up to 1.2K. It was found that (at a given liquid level) the best ion signals were obtained from both the long and short cell when the voltage between the source S and ground were the same. Also, other voltages could be varied as long as this source to ground voltage remained constant and the ion signal amplitudes would not change. This implies that the glow discharge, which depends on this voltage (and the liquid level) is associated with the creation of this new ion complex.

Reproduced with permission of the copyright owner. Further reproduction prohibited without permission.

Qualitatively new phenomena appear when the liquid level is placed at the source grid. The normal negative ion pulse becomes very strong, the fast ion pulse becomes very weak, and a series of pulses with intermediate transit times appears. These signals appear to be due to genuine charged particles traversing the drift region. Their transit time through the cell varies with drift electric field and temperature in a reasonable fashion. We believe that lowering the liquid level changes the discharge making conditions suitable for creation of the intermediate ions.

Under all run conditions, when polarities in the cell are reversed we observe only the single, usual, positive ion pulse; no anomalous positive carriers have been detected in these experiments.

D. Data and Analysis

With careful adjustment of the liquid level and the intensity of the glow discharge, weak field mobility data can be obtained for all the carriers. Strong electric fields in the drift region are not required to produce the newly discovered ions.

Representative data traces for the fast and intermediate ions are shown in Figs. 14 and 15. The fast ion signals are easy to control and quite good data have been obtained. The intermediate ion data are not as good, due to the difficulty in controlling the signal strength. Note the extremely short gate pulse used to separate the various intermediate ion signals. We do not believe that all

Reproduced with permission of the copyright owner. Further reproduction prohibited without permission.

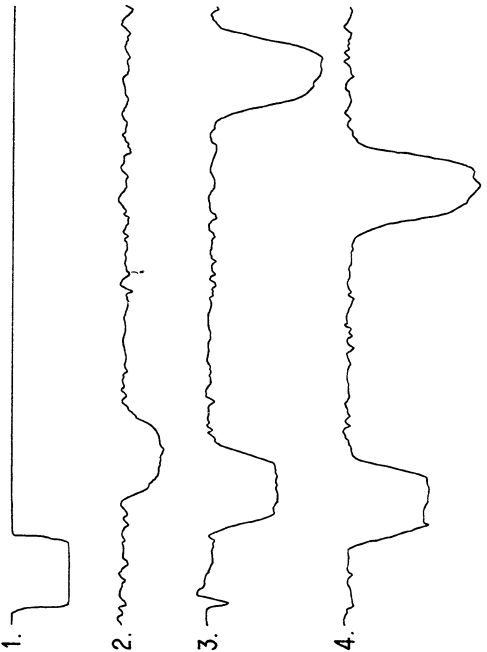

Fig. 14. Sample data traces showing the fast and normal negative pulses. Trace 1 is the gate pulse from the pulse coupler. Traces 2, 3, and 4 are data taken for increasing drift field at constant temperature. The trace length represents 0.010 sec and the vertical axis is collected current. The normal negative carrier is too slow to appear on trace 2.

Reproduced with permission of the copyright owner. Further reproduction prohibited without permission.

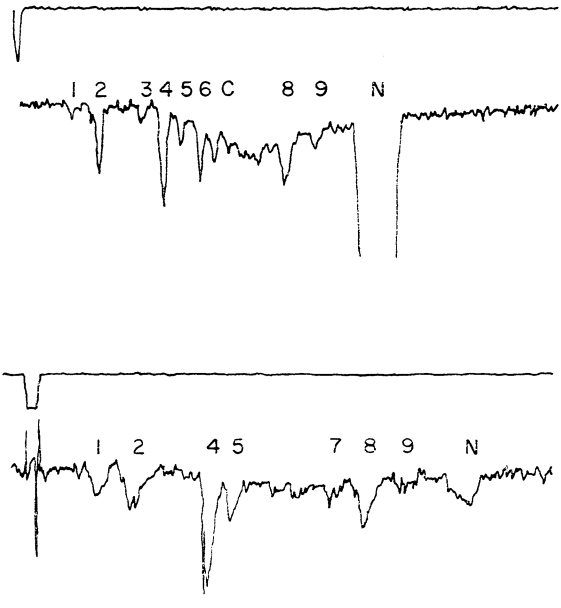

Fig. 15. Data traces showing the intermediate ion signals. Each set gives the gate pulse and resulting ion spectrum. The labels match those of Fig. 18, N = normal ion and 1 = fast ion. Upper traces: 6.5 cm cell, T = 1.005K, drift field = 200V, trace length = 0.08 sec. Lower traces: 2.6 cm cell, T = 0.989K, drift field = 100V, trace length = 0.02 sec.

Reproduced with permission of the copyright owner. Further reproduction prohibited without permission.

intermediate ions have been resolved.

Fast ion velocities are plotted against drift electric field for several temperatures in Fig. 16. As examination of these curves indicates, weak-field mobilities could be obtained whenever ion velocities were kept below 8 m/sec. Figure 17 shows the fast ion's mobility plotted against reciprocal temperature (the error bars are at the 90% confidence level). The data were taken in both short cells, one using a tritium β source and the other the "shower head I" source.

The best intermediate ion data from two runs in the long cell are given in Fig. 18. Normal and fast ion data taken in the same run are also shown. Although the best conditions for studying the intermediate ions are not optimal for the normal and fast negative carriers, the agreement with data taken in the short cell (Fig. 17) is excellent. Also the intermediate ion data taken in the short cell agree with the long cell data, although the short-cell signals are not as good.

Table 1 gives the computer best fit slope for each ion. The slopes are between 8.5K and 11.2K, suggesting the dominance of rotons in the scattering processes. This table also gives an approximate bubble radius for each ion. They were derived by assuming $\mu \propto R^{-2}$ (Brody 1970) and $R = \sqrt{\mu_N/\mu}\, R_N$, where R and μ are the radius and mobility of the bubble. The subscript N denotes normal electron bubble quantities. Note that we get a bubble

Reproduced with permission of the copyright owner. Further reproduction prohibited without permission.

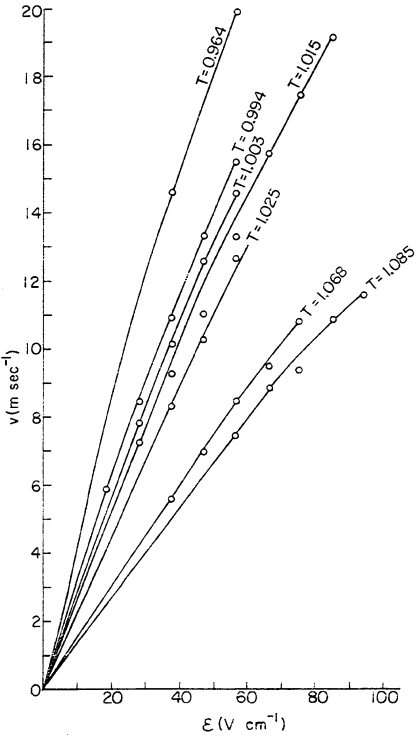

Fig. 16. Fast ion velocity v plotted against drift electric field $\mathcal{E}$ for temperatures from T = 0.964 to T = 1.085K. The curves have been drawn through zero.

Reproduced with permission of the copyright owner. Further reproduction prohibited without permission.

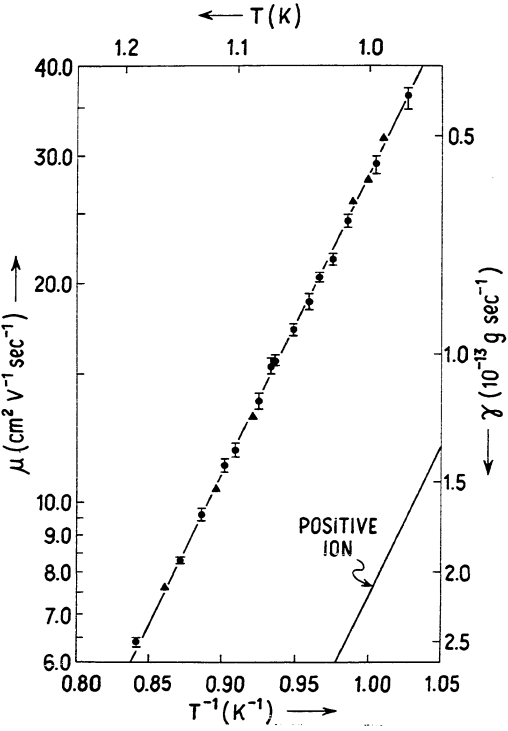

Fig. 17. Mobility μ plotted against reciprocal temperature T^{-1} for the fast negative carrier. The circles and triangles denote data taken in the two 2.6 cm cells, one using a β source and the other the shower head I source. The positive ion μ is also shown (Donnelly 1967).

Reproduced with permission of the copyright owner. Further reproduction prohibited without permission.

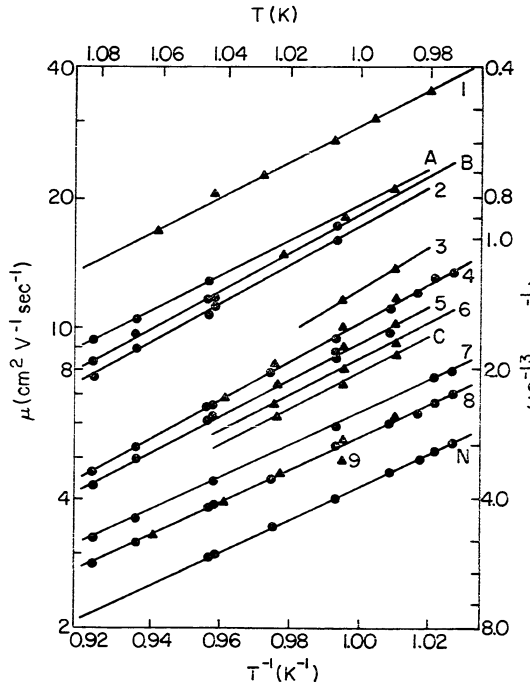

Fig. 18. Fast (1), intermediate, and normal (N) negative carrier mobilities μ (and friction coefficient γ) plotted against reciprocal temperature T^{-1} (and temperature T). The data are from two runs in the 6.5 cm cell using the shower head II source.

Reproduced with permission of the copyright owner. Further reproduction prohibited without permission.

Table 1

Ion	Computer best-fit slope to data (K)	Bubble Radius $R \approx \sqrt{\frac{4m}{M}}\, R_N$ (Å)
1	9.4	6.2
A	9.3	7.5
B	10.2	7.9
2	10.3	8.1
3	11.2	10.1
4	10.1	10.4
5	9.6	11.0
6	9.5	11.5
C	9.6	12.0
7	8.5	13.2
8	8.5	14.2
N	8.6	16.1

Reproduced with permission of the copyright owner. Further reproduction prohibited without permission.

radius for the fast ion of about 6.2 Å. This is close to, but slightly larger than the positive ion, suggesting that a snowball does not form.

Examination of the normal positive and negative ion data shows that a bubble has a higher mobility than a snowball of the same size (Brody 1970). It would appear that these new fast carriers have as high a mobility as any bubble or snowball-type charge carrier can have; if a bubble were any smaller it would form a snowball and its mobility would fall drastically.

E. Possible Models

Several experiments and a good deal of thought and speculation have been done inquiring into the structure of the new carriers. We discuss possible structures below:

1. Free Electron

The mobility measurements indicate that none of these species is a free ("conduction band") electron, since theory predicts a much higher mobility (by two orders of magnitude). Also, at the modest drift fields employed here, a free electron is expected to form a bubble state in a very short time.

2. Heavy Impurity Ion

The snowball model and the Baym, Barrera, and Pethick theory (substantiated for positive ions by our K^+ experiment) predict that any heavy ion, positively or negatively charged, will have a mobility very near that of the normal positive ion. From Fig. 18 it can be seen that the ions labeled

Reproduced with permission of the copyright owner. Further reproduction prohibited without permission.

C ($\Delta\mu/\mu$ = -0.06) and 7 ($\Delta\mu/\mu$ = 0.2) have mobilities closest to the positive helium ion mobility. The K^+ experiment would indicate that both these mobility differences are too large to be due to mass corrections. In the case of ion C the correction is of the wrong sign. We conclude that none of these new charge carriers is a heavy impurity.

3. Excited Electron Bubble State

The cavity an electron carves out in liquid helium is due to its high zero-point energy. Therefore electrons in higher energy states should produce larger bubbles, which should have smaller mobilities. None of the new charge carriers is slower than the normal negative carrier, indicating that an excited electron bubble has not been observed.

4. Two-Electron Bubble

Dexter and Fowler (1969) have theoretically treated the two-electron bubble in liquid helium. Their variational calculations show that this complex would have an energy almost 0.5 ev above the energy of two one-electron bubbles. The $2e^-$ bubble radius is found to be about 30 Å. Therefore, this complex is expected to be unstable and possess a mobility lower or comparable to the normal negative complex mobility. All of the new carriers are long lived and have a higher mobility than the normal one-electron bubble.

5. He^3 Dependent State

Since He^3 is known to collect on He^4 liquid surfaces

Reproduced with permission of the copyright owner. Further reproduction prohibited without permission.

(Andreev 1966 and Zinovyeva and Boldarev 1969), the several carriers might be bubbles with more or less He^3 on their surfaces (Lekner 1970). To test any relation to He^3, we raised the He^3 concentration from the natural abundance to 100 ppm without effecting the ion signals. We also filled the cell through a Vycor superle k with a λ-transition temperature of 1.5K. Presumably He^3 and other impurities will be filtered from the liquid in the cell. Neither the fast, intermediate, nor normal negative carrier was affected.

6. States of He^-

Some or all of the new ion complexes might be related to the negative helium ion. This is known to occur in vacuum in a $(1s)(2s)(2p)\,^4P$ state, bound by 0.08 ev relative to a $2\,^3S$ metastable atom and a free electron (Brehm, Gusinow, and Hall 1967 and Oparin, Il'in, Serenkov, Solov'ev, and Fedorenko 1970). This system would presumably carve a smaller cavity in the liquid than does the free electron (Hill, Heybey, and Walters 1971 and Hickman and Lane 1971), resulting in a higher mobility. The various substates of the ^4P complex might form bubbles of different geometry, and have different mobilities. The source conditions which favor the production of these new ion complexes would be expected to lead to production of metastables in the vapor and a surface layer charged with electrons, which might efficiently produce these ions by the reaction $He^* + e^- \rightarrow He^-$, in the presence of other bodies to absorb the energy released.

Reproduced with permission of the copyright owner. Further reproduction prohibited without permission.

We have tried to test this possibility in several ways. (i) The $^4P_{5/2}$ substate decays in vacuo by Auger emission of an electron in an f-wave with a lifetime of 345 μsec, whereas the fine structure states of smaller J can decay by emitting a p-wave electron, and have a considerably shorter lifetime (11 μsec) (Blau, Novick, and Weinflash 1970 and Simpson, Browning, and Gelbody 1971). We have observed the new carriers to be stable for flight times of more than 10 msec, with no evidence of decay into a free electron (which would quickly form a bubble). If these carriers are identified with the negative helium ion, the Auger decay process must be inhibited in the liquid. (ii) Furthermore, the lifetime of the free ion is drastically shortened by application of a static magnetic field of a few hundred gauss, which mixes the long and short lived states (Blau, Novick, and Weinflash 1970). We have observed the new carriers in the presence of magnetic fields up to 1.2 kG[8], without any differential reduction of their signals relative to the normal one. (iii) Finally, energetic neutral excitations are known to be stable in liquid helium, but they are efficiently quenched by the addition of impurities (Surko, Packard, Dick, and Reif 1970). The He^- ion in the liquid, having nearly the same energy, would also be expected to quench. We have admitted up to 1000 NTP cm^3 of air to the lead tube connecting the cell with room temperature without observing any change in the intensity of the new signals. We have no way of know-

Reproduced with permission of the copyright owner. Further reproduction prohibited without permission.

ing how much material reaches the liquid during this procedure. However, when a slug of air is added to the cell, the temperature in the cell rises appreciably indicating that some of the hot air does reach the liquid. As was mentioned earlier, the cell was also filled through a superleak, eliminating all impurities, with no noticeable effect.

F. Conclusion

The above experiments have determined the mobilities of several new ion carriers in liquid helium. The conditions for their production have been described although the production process is not understood. Some possible structures for these new charge carriers have been ruled out, while others are still in question. The actual nature of these ions is still unknown.

Measurements on the effective masses and the photo-ejection spectra of these new ions might help reveal their structures. These experiments, difficult in themselves, would be even more challenging due to the production techniques required by the new ions. At present it is impossible to isolate a single new ion. Nature has made this new-found puzzle exciting but intricate.

Reproduced with permission of the copyright owner. Further reproduction prohibited without permission.

V. ROTON KINEMATICS AND ION-ROTON SCATTERING

A. Introduction

In analyzing the friction experienced by a charged particle in liquid helium it has been customarily assumed that the roton-ion scattering cross section is approximately geometrical. It is often assumed, for example, that this cross section is sufficiently weakly dependent on roton momentum that its variation over the range of thermally occupied roton states can be neglected. The cross section can be replaced by its average value and regarded as constant in performing integrals over the roton momentum distribution (see Chapter I. C.). This assumption has been adhered to in spite of the fact that the nature of the dispersion curve near the roton minimum implies very novel kinematic properties for the roton.

In this chapter we will analyze the mechanics of rotons and their scattering by a central force field. This will lead to a calculation for the ion-roton scattering cross section where the roton is considered to be a point. First classical roton mechanics are considered. When needed, a quantum mechanical point of view will be taken. The classical approximation is expected to be valid in cases where the forces vary slowly on the scale of the roton wavelength $\left\{ \frac{p_0}{\hbar} = k_0 = \frac{2\pi}{\lambda} \approx 2\text{Å}^{-1} \right\}$. If b is an important impact parameter, than we will be in the classical region when $k_0 b \gg 1$ (a condition readily

Reproduced with permission of the copyright owner. Further reproduction prohibited without permission.

satisfied by impact parameters comparable to the ion radii)[9]. At any rate, as will be seen below, analysis of the classical mechanical behavior of a roton is entertaining in itself.

B. Classical Roton Mechanics

We will regard the energy-momentum relation for an excitation near the minimum of the Landau dispersion curve as a classical Hamiltonian function. The Landau relation is

$$\varepsilon = \frac{(k-k_0)^2}{2\mu_r} + \Delta$$

where $k = \sqrt{k_x^2 + k_y^2 + k_z^2}$ is the magnitude of the momentum vector. Later, it will be convenient to use a rationalized form of this Hamiltonian[10]:

$$\varepsilon = \frac{(k-k_0)^2}{2\mu_r} \cdot \frac{(k+k_0)^2}{(k+k_0)^2} + \Delta$$

$$\approx \frac{(k^2-k_0^2)^2}{8\mu_r k_0^2} + \Delta$$

The group velocity of the excitation is given by $\vec{v}_g = \vec{\nabla}_k \varepsilon$, a result equivalent to the canonical equations $\dot{q}_i = \frac{\partial \mathcal{H}}{\partial p_i}$ with $\varepsilon(k,r) = \mathcal{H}(p,q)$. We note that rotons above/below the minimum have velocities parallel/antiparallel to their momentum:

$$\vec{v} = \frac{1}{2\mu_r} \vec{\nabla}_k \varepsilon = \frac{(k-k_0)}{\mu_r} \hat{k} \ ,$$

where Δ may be a function of position but not of momentum. Note that the "kinetic energy" $T = \frac{(k-k_0)^2}{2\mu_r}$ is equal to $\frac{1}{2}\mu_r v^2$.

Reproduced with permission of the copyright owner. Further reproduction prohibited without permission.

If Δ is a function of position our Hamiltonian will be also. We will assume the validity of the second type of canonical equation

$$\frac{\partial \mathcal{H}}{\partial q_i} = -\dot{p}_i \quad \text{or} \quad -\vec{\nabla}\Delta(r) = \vec{F} = \frac{d\vec{p}}{dt} .$$

Thus a force parallel with $\vec{p}$ will always cause p to increase. This will cause an increase in velocity and "kinetic energy" if $k > k_0$, but will decrease these quantities if $k < k_0$. This is expected in the second case, where $\vec{p}\cdot\vec{F} > 0$ implies $\vec{v}\cdot\vec{F} = \frac{dT}{dt} < 0$. This means that the trajectories of rotons in a central force field with momenta on opposite sides of the minimum will be quite different. For an attractive force field $(\frac{\partial \Delta}{\partial r} < 0)$ the two trajectories are diagrammed in Fig. 19. We will call the portion of the dispersion curve with $k > k_0$ the Ordinary branch and the part with $k < k_0$ the Extraordinary branch. As the roton minimum is approached from either side the group velocity goes to zero, implying that rotons with k near k_0 are moving very slowly. A force field may scatter these rotons strongly.

Finally, we note the dispersion curve is double-valued. That is, for a given energy there are two distinct momentum magnitudes which a roton may possess. This means that a roton can convert from one branch to another while being elastically scattered, the magnitudes of the initial and final momenta being unequal (Fetter 1968). A roton will convert from one branch to the other if its momentum passes

Reproduced with permission of the copyright owner. Further reproduction prohibited without permission.

Reproduced with permission of the copyright owner. Further reproduction prohibited without permission.

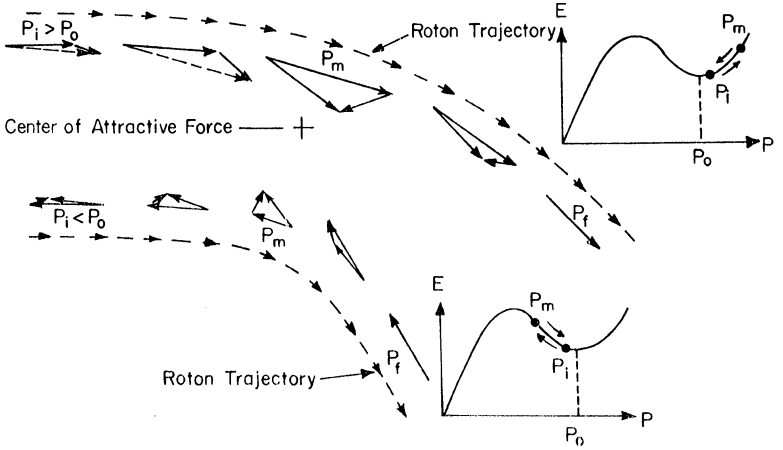

Fig. 19. Trajectories of Ordinary and Extraordinary rotons scattered by an attractive potential with vector diagrammed momentum changes. P_i = initial roton momentum and P_f = final roton momentum; $P_i = P_f$. P_m = maximum (Ordinary branch) or minimum (Extraordinary branch) roton momentum during the scattering process. The dispersion curve showing the locus of momenta is given for each case.

through the roton minimum. As was seen in Fig. 19, an attractive force drives the roton's momentum away from the minimum -- a repulsive force is needed for conversion. A hard sphere is an infinite repulsive force, and conversion can occur in hard sphere scattering.

We now consider the four types of scattering illustrated in Fig. 20. The upper two pictures show rotons which always remain on the same branch of the dispersion curve whether or not they strike the hard core (Normal process). The lower two diagrams show rotons which convert to the opposite branch after striking the hard core (Anomalous process). In the first two cases the momentum transfer is the same as in billiard-ball collisions, while in the last two cases an unusually small amount of momentum is transferred. In Anomalous-Extraordinary scattering, the momentum transfer is in a direction opposite to the roton momentum. This results in a negative momentum transfer cross section.

C. Momentum Transfer Cross Section

1. General Scattering

When considering the friction a particle encounters propagating through a medium, the differential cross section describing the scattering process involved must be weighted by the momentum transfer. The appropriate quantity is the momentum transfer cross section

$$\sigma_m(k) = \int_{\text{all angles}} \frac{1}{k}\,\hat{k}\cdot(\vec{k}-\vec{k}')\,\frac{d\sigma(\alpha,k)}{d\Omega}\,d\Omega$$

Reproduced with permission of the copyright owner. Further reproduction prohibited without permission.

Reproduced with permission of the copyright owner. Further reproduction prohibited without permission.

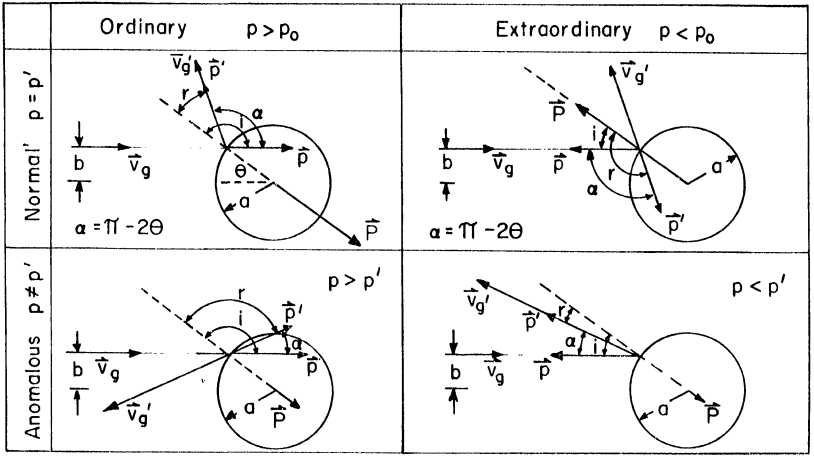

Fig. 20. The four possible cases of roton scattering off a hard sphere of radius a. Initially, the roton is incident from the left with group velocity v_g, momentum p, and impact parameter b. Primed quantities refer to the roton after the collision. i, r, and α are the incident, reflected, and scattered angles of the roton momenta. P = momentum transferred to the sphere, $\alpha = |i-r|$, $\ell = p \cdot \sin(i) = p' \cdot \sin(r) = \ell'$, P = $p \cdot \cos(i) - p' \cdot \cos(r)$.

where k and k' are the initial and final momentum of the scattered particle in the rest frame of the scattering particle. This expression can be derived following the arguments of Baym, Barrera, and Pethick (1969), but assuming that the initial and final momenta of the scattered excitation have unequal magnitudes[11].

2. Classical Scattering

Treating roton mechanics classically, for a spherically symmetric scattering potential we have

$$\sigma_m(k) = \int_{\text{all } b} 2\pi \left(1 - \frac{k'}{k}\cos\alpha\right) b\, db$$

where b is the roton impact parameter. As can be seen in Fig. 20, α is the angle between the incident and scattered roton momenta. In all four types of scattering α can be obtained by doing the classical orbit integral numerically when Δ is a function of position.

3. Classical Turning Point

To calculate $\sigma_m(k)$ we need the angle α for all incident roton impact parameters at a given initial value of roton momentum. The orbit integral (Goldstein 1950) gives the classical angle of impact or turning point Θ of the roton, from which α is derived (see Fig. 20). The two cases of Normal scattering require doing this integral once since $\alpha = \pi - 2\Theta$. The anomalous cases need the integral done once for each branch, the two pieces then being fitted together to form the unusual trajectory and determine the angle α.

Reproduced with permission of the copyright owner. Further reproduction prohibited without permission.

For rotons with total energy $\mathcal{E}$ and angular momentum $\ell = \hbar k$ held fixed, the orbit integral is

$$\pi - \theta = \int_{r_0}^{\infty} \frac{\hbar}{r} dr = \hbar k \int_0^{u_0} du \left\{ 2\mu_r [\mathcal{E} - \Delta(u)] - (\hbar k u)^2 + k_0^2 + 2k_0 \sqrt{2\mu_r [\mathcal{E} - \Delta(u)]} \right\}^{-1/2}$$

where $u = 1/r$

k = initial roton momentum at $r = \infty$ $(u = 0)$

k_0 = momentum at roton minimum

$\hbar$ = roton impact parameter

u_0 = reciprocal radius of the roton's closest approach or turning point (r_0)

and $\mathcal{E}$ = roton energy (with Δ allowed to vary with position).

After determining $\alpha(k, \hbar)$ from the orbit integral, the integral for the momentum transfer cross section can be done numerically. The result is $\sigma_m(k)$, a function of the roton's initial momentum. When this procedure is followed for Normal scattering from a hard sphere (Δ held constant), we obtain $\sigma_m^{ON} = \sigma_m^{EN} = \sigma_g = \pi a^2$, indicating that the calculations are being done correctly. The subscripts N, O, and E stand for Normal, Ordinary, and Extraordinary types of scattering. Later, A will denote Anomalous scattering (see Fig. 20).

4. Anomalous Hard Sphere Scattering

In Anomalous hard sphere scattering the incident angle (i) and reflected angle (r) are not related by $r = \pi - i$, as in Normal Scattering (Fig. 20). From conservation of

Reproduced with permission of the copyright owner. Further reproduction prohibited without permission.

angular momentum or continuity of the roton wave vector parallel to the surface of the hard sphere, we have

$$k \sin(i) = k' \sin(r) \quad \text{or} \quad \sin(r) = \frac{k}{k'} \sin(i).$$

If k is greater than k_0, then $k/k' > 1$, and the incident angle for which $k/k' \sin(i) = 1$ is the largest angle for which Ordinary-Anomalous scattering can occur. At larger angles the scattered particle would have to go through the hard core. There is no restriction on incident angle in Extraordinary-Anomalous scattering ($k < k_0$) since $k/k' < 1$.

For k very near k_0, this asymmetry becomes less important and the momentum transfer cross section is approximately antisymmetric:

$$\sigma_m^{OA} \approx 2 \frac{|\delta k|}{k} \sigma_g \quad \text{and} \quad \sigma_m^{EA} \approx -2 \frac{|\delta k|}{k} \sigma_g$$

or $\sigma_m^A \approx 2 \frac{\delta k}{k} \sigma_g$ where $\delta k = k - k_0$ is small.

Define $\rho = k'/k$, the ratio of final and initial roton momenta. Then for all δk we have

$$\sigma_m^{OA} = \sigma_g \left[\rho^2 (1-\rho^2/2) - 1/8 (1-\rho^2)^2 \ln\left(\frac{1-\rho}{1+\rho}\right) - 1/4 \rho (1+\rho^2) \right]$$

and

$$\sigma_m^{EA} = \sigma_g \left[1/2 - 1/4 \rho (1+\rho^2) - 1/8 (1-\rho^2)^2 \ln\left(\frac{\rho-1}{\rho+1}\right) \right].$$

A graph of σ_m^A plotted against roton momentum k for anomalous hard sphere scattering is shown in Fig. 21. Note the asymmetry about k_0.

D. Particle Fluxes for Hard Sphere Scattering

Classically there is no way to determine what will happen to a roton after it scatters off the hard core.

Reproduced with permission of the copyright owner. Further reproduction prohibited without permission.

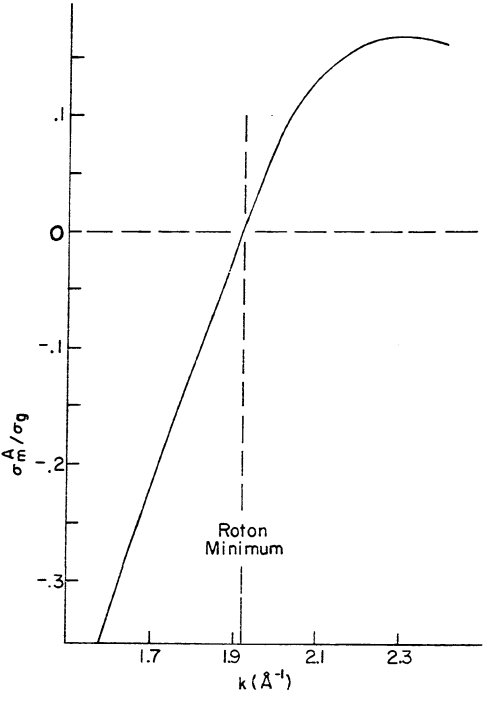

Fig. 21. Anomalous, hard sphere momentum transfer cross section σ_m^A (normalized to the geometric cross section σ_g) vs. initial roton wave number k.

Reproduced with permission of the copyright owner. Further reproduction prohibited without permission.

We can not calculate the relative strengths of Normal and Anomalous scattering, if both branches are possible. The problem is similar to that of a light wave passing from one medium to another, where the index of refraction changes discontinuously. When a single beam of light strikes the interface both a reflected and a transmitted beam result. The reflected light and the Normally scattered roton beams are analogous as are the transmitted (but refracted) light and Anomalously scattered roton beams. The analogy can be seen by considering the vector-momentum diagram of the scattering, shown in Fig. 22(a).

We seek now to calculate the particle fluxes for scattering into the Normal and Anomalous channels. This is done by solving the Schrodinger equation using the Hamiltonian presented in Section B. If $\vec{k}$ is replaced by $-i\vec{\nabla}$ in the Landau relation, the resulting expression is not a differential operator. But letting $\vec{k}$ go to $-i\vec{\nabla}$ in the rationalized energy expression of Section B yields a Hamiltonian which is a differential operator and is fourth order in $\vec{\nabla}$. This means that for a roton incident on a hard sphere, there are two possible scattering channels. In the case of an infinite potential barrier (the hard core), the boundary conditions may be found in the usual manner (Schiff 1955) starting with a finite potential which is allowed to become infinite. The boundary conditions are that the wave function and its first normal derivative go to zero at the surface of a hard core[12]. Consider rotons incident on a

Reproduced with permission of the copyright owner. Further reproduction prohibited without permission.

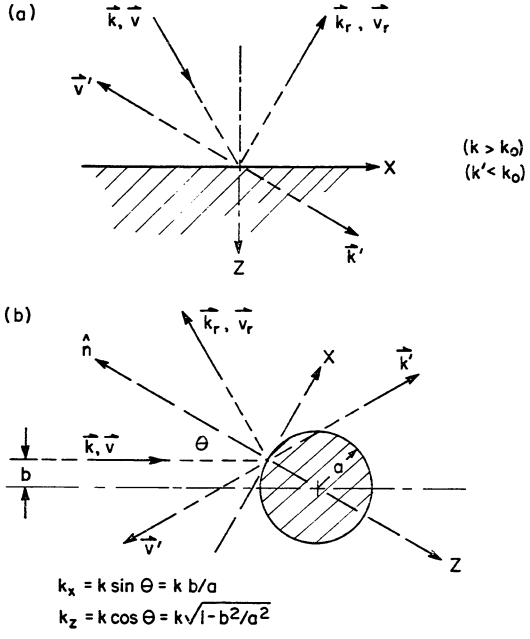

Fig. 22. (a) Two dimensional scattering off a plane surface (infinite potential). The subscript r denotes Normal scattering and the primes identify Anomalous scattering. The case for $\rho<1$ is shown. (b) The same scattering problem as (a) in spherical geometry. The roton impact parameter is b.

Reproduced with permission of the copyright owner. Further reproduction prohibited without permission.

plane. The wave function is of the form

$$\psi = e^{-i\vec{k}\cdot\vec{x}} + \alpha_N e^{i\vec{k}_r\cdot\vec{x}} + \alpha_A e^{i\vec{k}'\cdot\vec{x}},$$

where k, k_r, and k' are the wave vectors for the incident, Normally scattered, and Anomalously scattered rotons. The momenta and velocities are diagrammed in Fig. 22(a). Using the boundary conditions

$$\psi(0) = \hat{n}\cdot\vec{\nabla}\psi(0) = 0,$$

the conservation of energy, and the requirement that all wave vectors be real (propagating waves), we get

$$\alpha_N = \frac{k_z - k_z'}{k_z + k_z'} \quad \text{and} \quad \alpha_A = \frac{-2k_z}{k_z + k_z'}.$$

We also obtain a condition which must be satisfied for Anomalous scattering to be possible: $k_x^2 \leq k_o^2 - \frac{1}{2}k_z^2$.

The fractions of rotons Normally and Anomalously reflected[13] are

$$\Gamma_N = \left(\frac{k_z - k_z'}{k_z + k_z'}\right)^2 \quad \text{and} \quad \Gamma_A = \frac{4k_z k_z'}{(k_z + k_z')^2}$$

In the small wave length limit, these same relations hold for scattering off a hard sphere. The relations used in the coordinate transformation are shown in Fig. 22(b).

Reproduced with permission of the copyright owner. Further reproduction prohibited without permission.

Using these we obtain

$$\Gamma_N = \frac{1-2\eta-2\sqrt{(1-\eta)(\rho^2-\eta)}+\rho^2}{1-2\eta+2\sqrt{(1-\eta)(\rho^2-\eta)}+\rho^2}$$

and

$$\Gamma_A = \frac{4\sqrt{(1-\eta)(\rho^2-\eta)}}{1-2\eta+2\sqrt{(1-\eta)(\rho^2-\eta)}+\rho^2} \quad ,$$

and $\eta \leq \rho^2$ for Anomalous scattering to be possible. In the above we have $\eta = b^2/a^2$ and $\rho = k'/k$. Note: conservation of particles is satisfied since $\Gamma_N + \Gamma_A = 1$.

For a given value of b (the roton impact parameter) Γ_N and Γ_A give the flux ratios for the Normal and Anomalous scattering channels as a function of roton momentum. The momentum transfer cross sections, which include all types of scattering, are as follows:

$$\sigma_m^0(k) = \int_0^{b_A} \sigma_m^{0N}(k,b)\,\Gamma_N\,db + \int_0^{b_A} \sigma_m^{0A}(k,b)\,\Gamma_A\,db + \int_{b_A}^{a} \sigma_m^{0N}(k,b)\,db$$

$$\sigma_m^E(k) = \int_0^{a} \sigma_m^{EN}(k,b)\,\Gamma_N\,db + \int_0^{a} \sigma_m^{EA}(k,b)\,\Gamma_A\,db \quad ,$$

where b_A is the maximum impact parameter for which Anomalous scattering is allowed. The integrals can be done analytically, and the results are

$$\sigma_m^0 = \sigma_g\left[\frac{1}{6(1-\rho^2)^2}\left(6-3\rho+12\rho^2-5\rho^3+11\rho^5-16\rho^6-3\rho^7+4\rho^8\right) - \tfrac{1}{4}(1-\rho^2)^2 \ln\left(\frac{1-\rho}{1+\rho}\right)\right]$$

$$\sigma_m^E = \sigma_g\left[\frac{1}{6(1-\rho^2)^2}\left(2-3\rho+4\rho^2-5\rho^3-6\rho^4+11\rho^5-3\rho^7\right) - \tfrac{1}{4}(1-\rho^2)^2 \ln\left(\frac{\rho-1}{\rho+1}\right)\right].$$

Reproduced with permission of the copyright owner. Further reproduction prohibited without permission.

Figure 23 shows these compared to pure Anomalous scattering. Pure Normal scattering gives the geometrical cross section, as mentioned earlier.

It is clear that if we treat an ion complex in liquid helium as a hard sphere, the roton's unusual properties result in a momentum transfer cross section which is strongly dependent on k and far from geometrical.

E. Ion-Roton Scattering

We have already shown the results of treating the roton as a point and the ion complex as a hard sphere. This treatment is applicable to both the e^- bubble and the positive helium snowball by adjusting the geometrical cross section σ_g in the previous equations.

As was stated in Chapter I. A., a charge in liquid helium polarizes the helium atoms around it, causing electrostriction of the medium. This produces a pressure gradient which, for the massive positive ion, reaches the melting pressure at a radius of 6 Å, a solid helium snowball being created inside this radius. The electron's high zero-point energy carves out a cavity in the liquid of 16 Å radius, which makes snowball formation impossible and leaves very little density gradient outside the bubble. We now consider the effect of this density gradient on ion-roton scattering. Both the position and curvature of the roton minimum are functions of fluid density (Henshaw and Woods 1961). That is $k_0 = k_0(r)$, $\Delta = \Delta(r)$ and $\mu = \mu(r)$ in the vicinity of the ion. We will only consider the variation

Reproduced with permission of the copyright owner. Further reproduction prohibited without permission.

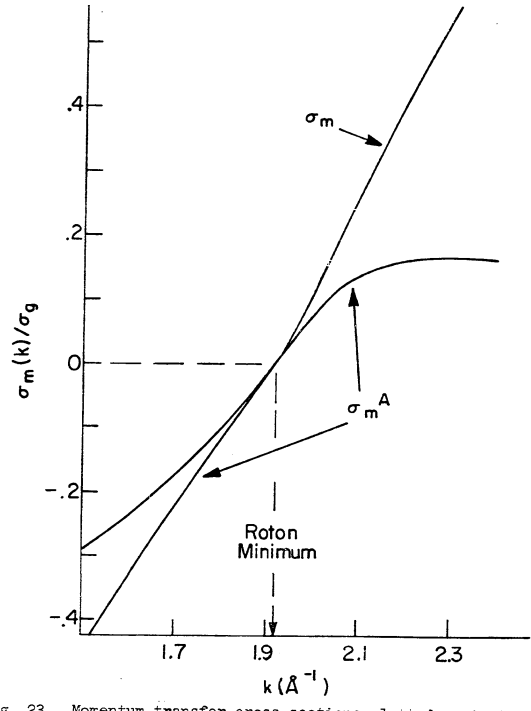

Fig. 23. Momentum transfer cross sections plotted against initial roton wave number for rotons scattering off a hard sphere of geometrical cross section σ_g . σ_m^A represents pure Anomalous scattering and σ_m includes both Normal and Anomalous scattering using the calculated particle flux ratios.

Reproduced with permission of the copyright owner. Further reproduction prohibited without permission.

of Δ with position. Inclusion of effects due to spatial variation in Δ will be seen to alter the hard sphere cross sections only slightly[14], except for k very near k_0.

As the liquid density increases, the roton activation energy Δ decreases (Henshaw and Woods 1961), so that rotons will see an attractive effective potential outside the positive ion snowball, which will be very weak outside the electron bubble. We will treat both the bubble and the snowball as inaccessible to the roton, or as hard sphere scatterers at 16 Å and 6 Å radii, respectively.

The roton is scattered by a spherically symmetrical scattering potential which, outside the hard core, can be written as $V(r) = \xi \Delta_0 \frac{\delta\rho}{\rho_0}$ (de Boer and 't Hooft 1961). The quantity ξ is the fractional change in Δ per unit fractional change in ρ ($\xi = \frac{\rho}{\Delta_0}\frac{\partial\Delta}{\partial\rho}$), and is not well known. The value of ξ will not be critical. Using linear interpolation between two points, ξ = -1 is obtained from neutron scattering experiments (Henshaw and Woods 1961). The vapor pressure neutron value of 8.68K will be used for Δ_0. The Atkins model is used to calculate $\delta\rho/\rho_0$. The balance between polarization forces and the pressure gradient around an ion yields the equation $\vec{\nabla} P = \frac{\rho}{m_4}\vec{\nabla}(\frac{1}{2}\alpha\mathcal{E}^2)$, which must be integrated. For ρ slowly varying we have

$$\int_{P_0}^{P} \frac{\vec{\nabla} P}{\rho} \approx \frac{P - P_0}{\rho_0} \qquad \text{and} \qquad \rho = \rho_0 + \frac{\partial\rho}{\partial P}(P - P_0).$$

This gives $\frac{\rho - \rho_0}{\rho} = \beta(P - P_0)$ where $\beta = \frac{1}{\rho}\frac{\partial\rho}{\partial P}$, the

Reproduced with permission of the copyright owner. Further reproduction prohibited without permission.

compressibility. Therefore $\frac{\rho - \rho_0}{\rho} \approx \frac{\delta\rho}{\rho_0} = \frac{1}{2}\frac{\rho_0}{m_{He}}\beta\alpha\mathcal{E}^2$.

We have $\alpha = 2\cdot10^{-25}$ cm^3 (helium polarizability)

$\beta = 1.2\cdot10^{-8}$ cm^2/dyne (helium compressibility)

$\frac{\rho_0}{m_{He}} = 2.2\cdot10^{22}$ (helium number density)

$\mathcal{E} = 4.8\cdot10^{-10}/r^2$ esu/cm^2 (ion electric field)

which yield $\delta\rho/\rho_0 = 6.1\cdot10^{-30}/r^4$ (r in cm).

Now $\Delta(r) = \xi\Delta_0\,\delta\rho/\rho_0 + \Delta_0$

$= \Delta_0 - 5.3\cdot10^{-45}/r^4$ (ergs) (r in cm)

$= \Delta_0 - 5.3\cdot10^{-13}/r^4$ (ergs) (r in Å).

Let $\frac{2\mu_r}{\hbar^2}[\Delta(r)-\Delta_0] = C_4/r^4$. Then $C_4 = \frac{2\mu_r}{\hbar^2}\xi\Delta_0 k_B\,\delta\rho/\rho_0$

or $C_4 = -112$ $1/r^4$ Å^2 (r in Å). So we have a r^{-4} potential, and in the units used in the orbit integral calculation the force constant is negative and of order 100.

Note that the ion's force field, represented by C_4u^4, is of importance in the orbit integral only when the potential energy of a roton in this field is on the order of its kinetic energy. This consideration yields the estimate

$$(k_\infty - k_0)^2 \approx \frac{C_4}{b^4} \quad \text{or} \quad \sigma_m = \pi b^2 \approx \frac{\pi\sqrt{C_4}}{|k_\infty - k_0|}$$

indicating that the momentum transfer cross section diverges at $k = k_0$. Including the r^{-4} potential with $C_4 = 90$ Å^2 in the orbit integral, we get the momentum transfer cross sections for Normal scattering, which are plotted against roton wave number in Fig. 24. The lower graph is for a hard core of 6 Å (appropriate for the positive ion) and the upper graph for a hard core of 15 Å (corresponding to the

Reproduced with permission of the copyright owner. Further reproduction prohibited without permission.

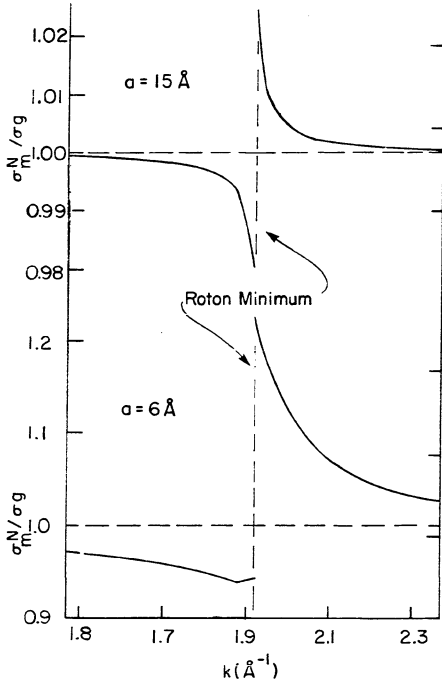

Fig. 24. Momentum transfer cross sections (σ_m) vs. initial roton momentum (k) for Normal ion-roton scattering. The force constant C_4 = 90 Å^2 and the curves are labeled by the value of the hard core radius a . Note the change in scale from top to bottom.

Reproduced with permission of the copyright owner. Further reproduction prohibited without permission.

electron bubble). It is clear that on the scale of the geometrical cross section, Normal scattering is not affected greatly by the attractive potential in either case. The Anomalous scattering is changed even less, there being no discontinuity or infinity at k_0, even for $a = 6$ Å.

To calculate the flux ratios in the presence of a force field around the ion requires an additional term in the energy equation. The magnitudes of the wave vectors at the hard core are altered from their values at infinity by the change in potential energy. The new energy conservation equation is

$$\frac{\hbar^2}{2\mu_r}(k-k_o)^2+\Delta_o=\frac{\hbar^2}{2\mu_r}\left[k(a)-k_o\right]^2+\Delta_o-\frac{C_4}{a^4}\cdot\frac{2\mu_r}{\hbar^2}\,.$$

This produces the following wave vector components at the hard core radius a

$$\left[k_z(a)\right]^2=\left(k_o+\delta k\sqrt{1+C_4a^{-4}\delta k^{-2}}\right)^2-k^2\sin^2\theta$$

$$\left[k'_z(a)\right]^2=\left(k_o-\delta k\sqrt{1+C_4a^{-4}\delta k^{-2}}\right)^2-k^2\sin^2\theta\,,$$

where $\delta k \equiv k-k_0$, k being the initial roton wave number. Using these relations to form new flux coefficients, and performing the integrals numerically yields σ_m, including the force field of the ion. The results for several force constants and hard core radii are plotted in Figs. 25, 26, and 27.

These cross sections are used with the Baym, Barrera, and Pethick (1969) formula to calculate the friction coefficient in the roton-dominated regime. Their result for

Reproduced with permission of the copyright owner. Further reproduction prohibited without permission.

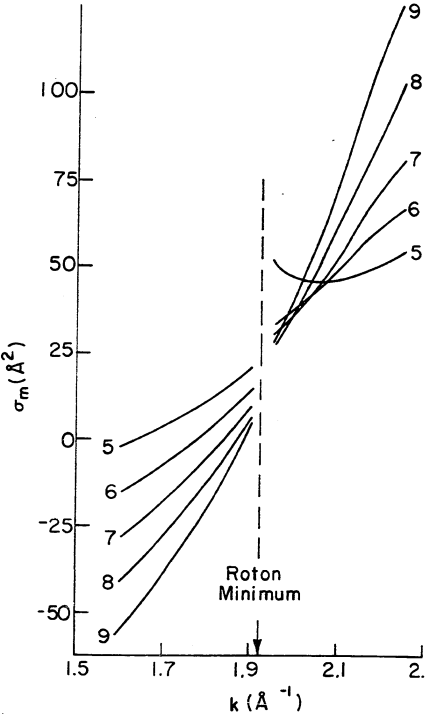

Fig. 25. Momentum transfer cross sections (σ_m) vs. initial roton momentum (k) for ion-roton scattering using the calculated flux ratios. The force constant is C_4 = 100 Å^2; the curves are labeled by the value of the hard core radius a.

Reproduced with permission of the copyright owner. Further reproduction prohibited without permission.

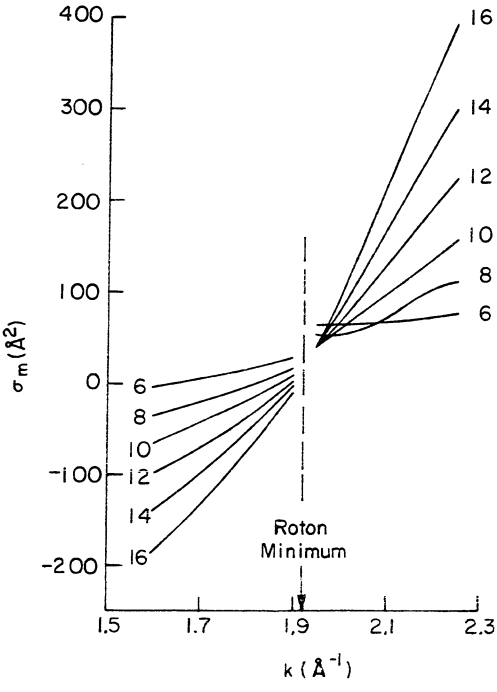

Fig. 26. Momentum transfer cross sections (σ_m) vs. initial roton momentum (k) for ion-roton scattering using the calculated flux ratios. The force constant C_4 = 200 Å^2; the curves are labeled by the value of the hard core radius a.

Reproduced with permission of the copyright owner. Further reproduction prohibited without permission.

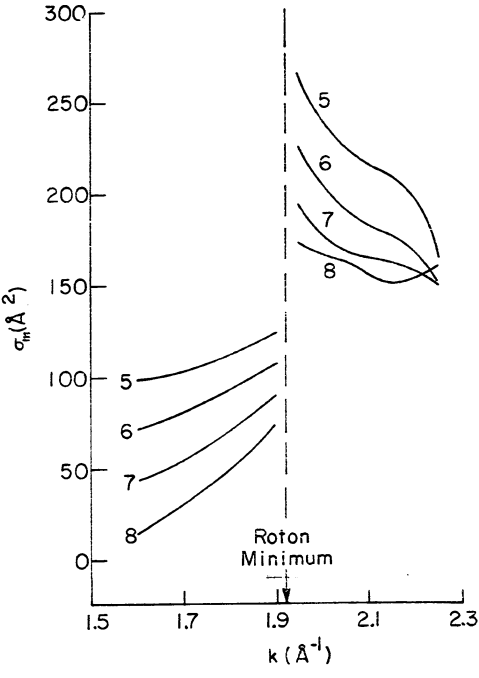

Fig. 27. Momentum transfer cross sections (σ_m) vs. initial roton momentum (k) for ion-roton scattering using the calculated flux ratios. The force constant C_4 = 1000 Å^2; the curves are labeled by the hard core radius a.

Reproduced with permission of the copyright owner. Further reproduction prohibited without permission.

the friction coefficient is

$$\gamma' = \frac{-\hbar}{6\pi^2}\int_0^\infty k^4 \frac{\partial n_k}{\partial k}\,\sigma_m(k)\,dk.$$

Since the rotons possess a Maxwellian distribution about k_0 (the roton energy gap being much larger than $k_B T$) we have

$$n_k = \exp\left[-\frac{\Delta}{k_B T} - \frac{\hbar^2 (k-k_0)^2}{2\mu_r k_B T}\right]$$

where k_B = Boltzmann's constant. Letting $k-k_0 = x$ and $k \to k_0$ we have

$$\gamma' = \frac{\hbar^3 k_0^4}{6\pi^2 \mu_r}\,\frac{e^{-\Delta/k_B T}}{k_B T}\int_{-\infty}^{\infty} |x|\, e^{-\frac{\hbar^2}{2\mu_r k_B T}x^2}\,\sigma_m(x)\,dx$$

Thus, the integral is the product of the momentum transfer cross section and the weighting function $|x|\, e^{-\frac{\hbar^2}{2\mu_r k_B T}x^2}$. The absolute value signs are needed since this term contains the group velocity of the roton, and must be positive (meaning the roton is initially travelling toward the ion) for scattering to occur. This weighting function is double-humped, and is plotted for a temperature of 1.5K in Fig. 28. The important contributions to the integral come from the region of the peaks of this distribution. Fortunately the region about k_0, where $\sigma_m(k)$ is so difficult to calculate on the computer (because of the discontinuity and apparent infinity) is unimportant.

A cross section independent of x can be obtained by averaging the values of $\sigma_m(x)$ at the two peaks in the distribution function. The results of this procedure for

Reproduced with permission of the copyright owner. Further reproduction prohibited without permission.

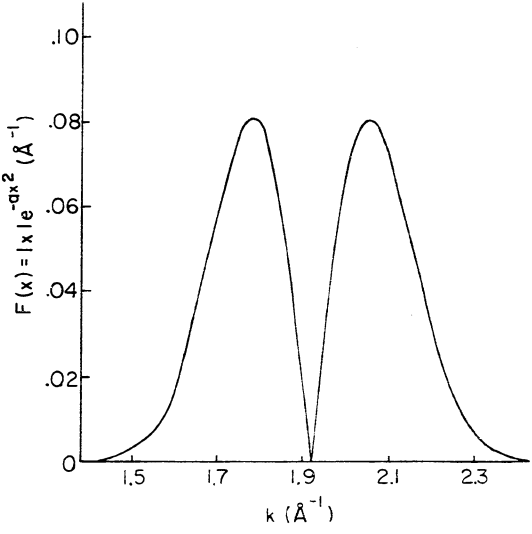

Fig. 28. The weighting function F(x) used with σ_m to obtain γ plotted against roton wave number k. $x = k-k_0$. $\alpha = \hbar^2/2\mu_r k_B T$, $|x_{peak}| = 0.115T^{\frac{1}{2}}$ Å^{-1}, a weak function of temperature.

Reproduced with permission of the copyright owner. Further reproduction prohibited without permission.

$T = 1.5K$ are listed in Table 2. The geometrical cross sections and the constant $\overline{\sigma}_m$ derived from the experimental data at $T = 1.5K$ are also given. The agreement is rather poor, discouraging us from doing the integral to obtain γ.

F. Conclusion

The most obvious deficiency of the theory is our neglect of the interactions between a roton and an impurity because of the dipole flow field associated with the roton. The assumption that the bubble and the snowball present the same boundary conditions to the roton is also questionable. We have also neglected the phonon portion of the dispersion curve. It is hoped that the preceeding ideas and calculations may prove helpful in formulating a correct theory of ion-roton scattering.

Reproduced with permission of the copyright owner. Further reproduction prohibited without permission.

Table 2

Hard Core Radius (Å)	$\sigma_g = \pi a^2$ (Å^2)	$\overline{\sigma_m}$ for $C_4 = 100$*	$\overline{\sigma_m}$ for $C_4 = 200$*	$\overline{\sigma_m}$ for $C_4 = 1000$*	$\overline{\sigma_m}$ from μ data* (Brody 1970)
5	77.5	27	47.5	167	
6	113	22.5	39	140	300 (snowball)
7	154	18.8	32	118	
8	209	18.8	27	103	
9	254	22			
10	314		28		
12	453		30		
14	616		30		
16	805		39		400 (bubble)

* T = 1.5K

Reproduced with permission of the copyright owner. Further reproduction prohibited without permission.

APPENDIX I

EXPERIMENTAL EQUIPMENT

	K^+ Experiment (Chapter III)	New Negative Ions Experiment (Chapter IV)
Vapor Pressure Measurements	Oil and Mercury Manometer	Type 1014A Electronic Manometer Datametrics Div., CGS Scientific Corp.
Resistance Thermometry	10^{-5} amp current Cubic Corp. Digital Volt Meter	10^{-7} amp current Doric DS-100 Digital Volt Meter
Pulse Generator	Types 160, 161, 162 Tektronix, Inc.	Data Pulse 100A Systron-Donner Corp.
Gate Pulse Isolation	Relay type W133MPCX-4 Magnecraft Electric Co.	Circuit of Fig. 11.
Cell Electrode Supplies	Batteries	Commercial Power Supplies except source which used batteries
Electrometer	Analog Devices P50LB 10^{10} ohm feedback resistor	Philbrick P25CH 10^{9} ohm feedback resistor
Signal Averager	Varian C-1024 Technical Measurement Corp.	Model 1062, with SD-3, SW-7, SD-2, SW-2 Plug-ins Fabri-Tek Instruments, Inc.

Reproduced with permission of the copyright owner. Further reproduction prohibited without permission.

APPENDIX II

MASS SPECTROMETER

A mass spectrometer was built to identify the positive ions emitted by hot tungsten wires. A diagram of the mass spectrometer is shown in Fig. 29. Ions from the hot wire are accelerated through a known potential difference and bent through 180 degrees at a 5 cm radius using a static magnetic field. Ion currents as large as 10^{-10} amp are detected by a Keithley 610BR electrometer and plotted against magnet current on an X-Y recorder. The instrument was calibrated by identifying peaks corresponding to known ions.

When a wire is first heated, many different ions are detected. After a short clean-up period, the K^{39+} and K^{41+} peaks are larger than all others by at least two orders of magnitude. The ratio of the two peak heights equals the known abundance ratio $\frac{N_{39}}{N_{41}} = 13.5$.

Reproduced with permission of the copyright owner. Further reproduction prohibited without permission.

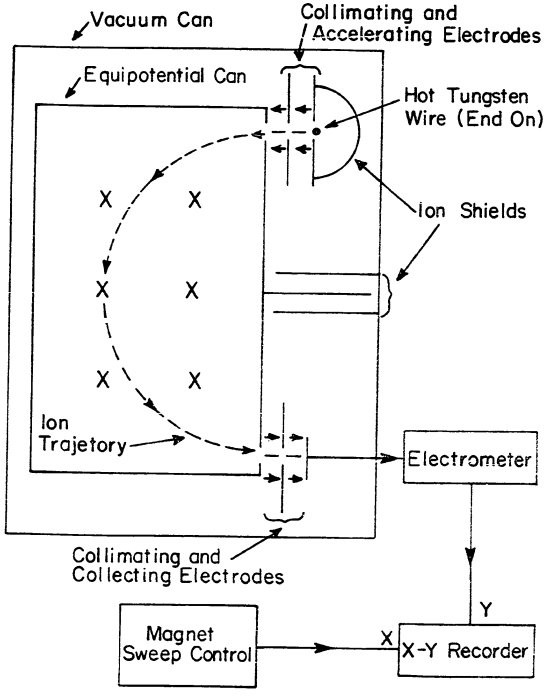

Fig. 29. Schematic diagram of the mass spectrometer and associated electronics. The magnetic field is going into the paper, denoted by X's.

Reproduced with permission of the copyright owner. Further reproduction prohibited without permission.

NOTES

1. A Hoke type 304A was used with an indium tinned needle. The pipe-fitting arms were cut off to save space.

2. Stycast 2850FT with catalyst 24LV made by Emerson and Cumming , Inc.

3. J. G. King (private communication) first suggested that a hot, potassium doped tungsten wire might work as a source of potassium ions in He II.

4. The grids were 70 lines per inch, 90% transmission made by Buckbee-Mears Co.

5. Microdot part number 031 0059 0001.

6. Microdot number 250-3919 special ordered with copper-clad shield.

7. R. Bowley (private communication) has done preliminary work on a theory of ion mobilities which includes the ionic mass.

8. The magnetic field was applied using a pair of water-cooled coils in the Helmholtz configuration mounted around the outside of the Dewar. The field at the cell was parallel to the path of the ions. The field was calibrated using a Hall probe in the Dewar in place of the cell.

9. Lifshitz and Pitaevskii (1958) found a quasi-classical approximation appropriate for treating roton-vortex line scattering.

10. A. L. Fetter, private communication.

11. T. M. Sanders, Jr., private communication.

12. T. M. Sanders, Jr., private communication.

13. T. M. Sanders, Jr., private communication.

14. In treating roton-vortex line scattering, Hall and Vinen (1956) found the variation of Δ with position unimportant compared to the $p \cdot \bar{v}_s$ term in the energy.

Reproduced with permission of the copyright owner. Further reproduction prohibited without permission.

BIBLIOGRAPHY

Andreev, A. F. (1966). Sov. Phys. JETP 23, 939.

Arkhipov, R. G. (1966), Sov. Phys. Uspekhi 9, 174.

Arkhipov, R. G. and Shal'nikov, A. I. (1960). Sov. Phys. JETP 10, 888.

Atkins, K. R. (1959). Phys. Rev. 116, 1339.

Baym, G., Barrera, R. G., and Pethick, C. J. (1969). Phys. Rev. Letters 22, 20.

Blau, L. M., Novick, R., and Weinflash, D. (1970). Phys. Rev. Letters 24, 1268.

Brehm, B., Gusinow, M. A., and Hall, J. L. (1967). Phys. Rev. Letters 19, 739.

Brody, B. A. (1970). Thesis (University of Michigan, Ann Arbor, Mi.).

Cade, A. G. (1965). Phys. Rev. Letters 15, 238.

Careri, G., Scaramuzzi, F., and McCormick, W. D. (1961). Proceedings of the VIIth International Conference on Low Temperature Physics, Ed. G. M. Graham and A. C. H. Hallett (University of Toronto Press, Toronto), p. 502.

Careri, G., Scaramuzzi, F., and Thomson, J. O. (1959). Nuovo Cimento 13, 186.

Cope, J. A. and Gribbon, P. W. F. (1967). Proceedings of the Tenth International Conference on Low Temperature Physics, Ed. M. P. Malkov (U.S.S.R.), p. 214.

Cunsolo, S. (1961). Nuovo Cimento 21, 76.

Dahm, A., Levine, J., Penley, J., and Sanders, T. M., Jr. (1961). Proceedings of the VIIth International Conference on Low Temperature Physics, Ed. G. M. Graham and A. C. H. Hallett (University of Toronto Press, Toronto), p. 495.

Dahm, A. J. and Sanders, T. M., Jr. (1966). Phys. Rev. Letters 17, 126.

Dahm, A. J. and Sanders, T. M., Jr. (1970). J. Low Temp. Phys. 2, 199.

Reproduced with permission of the copyright owner. Further reproduction prohibited without permission.

Date, M., Hori, H., and Kamata, H. (1971). Proceedings of the Twelfth International Conference on Low Temperature Physics, Ed. Eizo Kanda (Academic Press of Japan, Tokyo), p. 93.

de Boer, J. and 't Hooft, A. (1961). Proceedings of the VIIth International Conference on Low Temperature Physics, Ed. G. M. Graham and A. C. H. Hallett (University of Toronto Press, Toronto), p. 510.

Dexter, D. L. and Fowler, W. B. (1969). Phys. Rev. 183, 307.

Doake, C. S. M. and Gribbon, P. W. F. (1969). Phys. Letters 30A, 251.

Donnelly, R. J. (1967). Experimental Superfluidity (University of Chicago Press, Chicago).

Douglass, R. L. (1964). Phys. Rev. Letters 13, 791.

Fetter, A. L. (1969). Lectures in Theoretical Physics, vol. XI-B, Ed. K. T. Mahamthappa and W. E. Brittin (Gordon and Breach, New York), p. 359ff.

Fowler, W. B. and Dexter, D. L. (1968). Phys. Rev. 176, 337.

Goldstein, Herbert. (1950). Classical Mechanics (Addison-Wesley, Reading, Mass.), p. 71.

Hall, H. E. and Vinen, W. F. (1956). Proc. Roy. Soc. (London) 238, 215.

Henshaw, D. G. and Woods, A. D. B. (1961). Proceedings of the VIIth International Conference on Low Temperature Physics, Ed. G. M. Graham and A. C. H. Hallett (University of Toronto Press, Toronto), p. 539.

Hickman, A. P. and Lane, N. F. (1971). Phys. Rev. Letters 26, 1216.

Hickson, A. and McClintock, P. V. E. (1971). Phys. Letters 34A, 424.

Hill, J. C., Heybey, O., and Walters, G. K. (1971). Phys. Rev. Letters 26, 1213.

Ihas, G. G. and Sanders, T. M., Jr. (1970). Phys. Letters 31A, 502.

Ihas, G. G. and Sanders, T. M., Jr. (1971). Phys. Rev. Letters 27, 383.

Kuper, C. G. (1961). Phys. Rev. 122, 1007.

Reproduced with permission of the copyright owner. Further reproduction prohibited without permission.

Lekner, J. (1970). Phil. Mag. 22, 669.

Lemieux, G. P. and Leonard, A. C. (1968). Mech. Eng. 3, 74.

Lifshitz, E. M. and Pitaevskii, L. P. (1958). Sov. Phys. JETP 6, 418.

McClintock, P. V. E. (1969). Phys. Letters 29A, 453.

Miyakawa, T. and Dexter, D. L. (1970). Phys. Rev. A 1, 513.

Onn, D. G. and Silver, M. (1971). Phys. Rev. A 3, 1773.

Oparin, V. A., Il'in, R. N., Serenkov, I. T., Solov'ev, E. S., and Fedorenko, N. V. (1970). ZhETF Pis. Red. 12, 237.

Parks, P. E. and Donnelly, R. J. (1966). Phys. Rev. Letters 16, 45.

Rayfield, G. W. (1968). Phys. Rev. Letters 20, 1467.

Reif, F. and Meyer, L. (1960). Phys. Rev. 119, 1164.

Schiff, L. I. (1955). Quantum Mechanics (McGraw-Hill, New York), p. 29.

Schwarz, K. W. and Stark, R. W. (1968). Phys. Rev. Letters 21, 967.

Schwarz, K. W. and Stark, R. W. (1969). Phys. Rev. Letters 22, 1278.

Simpson, F. R., Browning, R., and Gilbody, H. B. (1971). J. Phys. B 4, 106.

Spangler, G. E. and Hereford, F. L. (1968). Phys. Rev. Letters 20, 1229.

Surko, C. M., Packard, R. E., Dick, G. J., and Reif, F. (1970). Phys. Rev. Letters 24, 657.

Williams, R. L. and Stacey, F. D. (1957). Can. J. Phys. 35, 928.

Yarnell, J. L., Arnold, G. P., Bendt, P. J., and Kerr, E. C. (1959). Phys. Rev. 113, 1379.

Reproduced with permission of the copyright owner. Further reproduction prohibited without permission.

Zinovyeva, K. N. and Boldarev, S. T. (1969). Proceedings of the Eleventh International Conference on Low Temperature Physics, Ed. J. F. Allen, D. M. Finlayson, D. M. McCall (University of St. Andrews Printing Department, St. Andrews), p. 367.

Zipfel, C. L. (1969). Thesis (University of Michigan, Ann Arbor, Mi.)

Zipfel, C. and Sanders, T. M., Jr. (1969). Proceedings of the Eleventh International Conference on Low Temperature Physics, Ed. J. M. Allen, D. M. Finlayson, and D. M. McCall (University of St. Andrews Printing Department, St. Andrews), p. 296.

Reproduced with permission of the copyright owner. Further reproduction prohibited without permission.